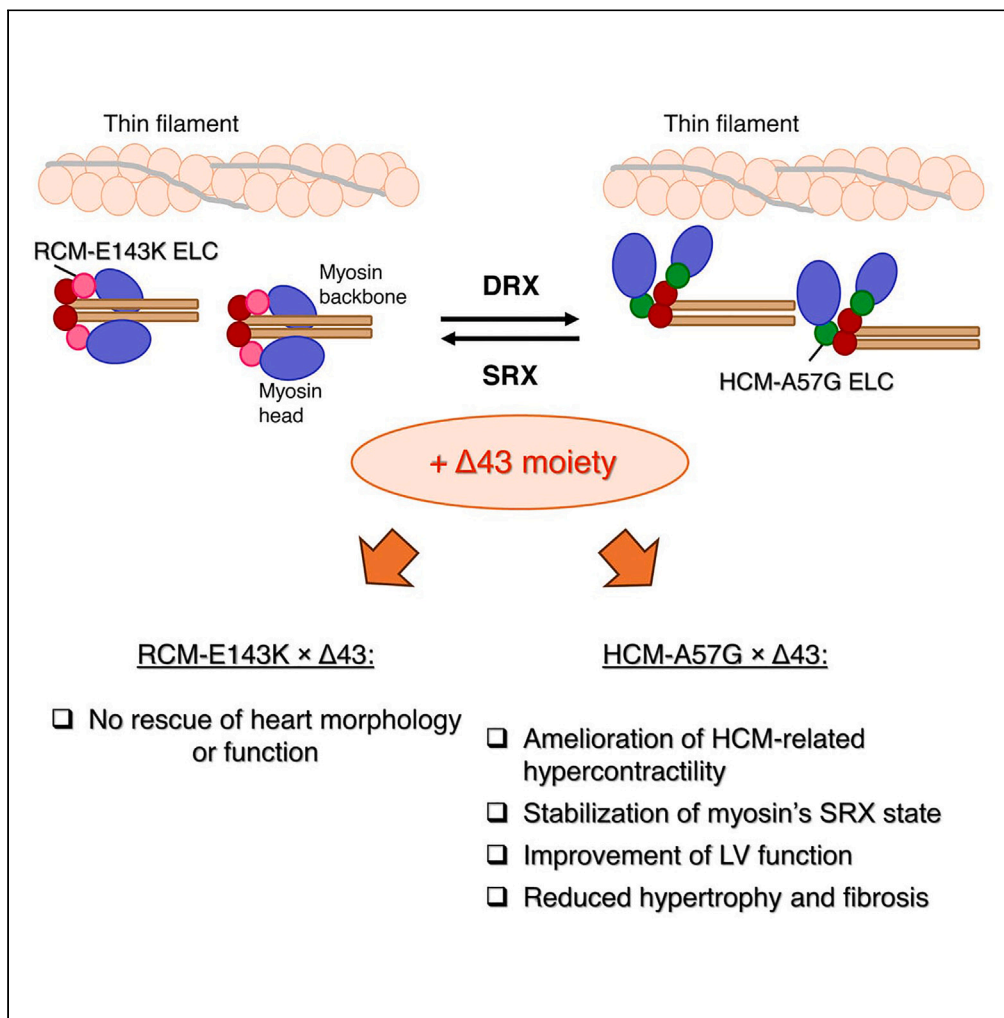# iScience

Article

Dual effect of N-terminal deletion of cardiac myosin essential light chain in mitigating cardiomyopathy

Yoel H. Sitbon, Katarzyna Kazmierczak, Jingsheng Liang, Andrew J. Kloehn, Judith Vinod, Rosemeire Kanashiro-Takeuchi, Danuta Szczesna-Cordary

dszczesna@med.miami.edu

Highlights

HCM and RCM ELC mutants cause heart pathology through different mechanisms

HCM-mutant destabilizes, while RCM-mutant favors myosin's SRX state

Deletion of N-ELC mitigates HCM but not RCM mutant heart dysfunction or fibrosis

N-ELC truncated Δ43 moiety has shown rescue properties to mitigate HCM

Article

Dual effect of N-terminal deletion of cardiac myosin essential light chain in mitigating cardiomyopathy

Yoel H. Sitbon,[1,2] Katarzyna Kazmierczak,[1,2] Jingsheng Liang,[1] Andrew J. Kloehn,[1] Judith Vinod,[1] Rosemeire Kanashiro-Takeuchi,[1] and Danuta Szczesna-Cordary[1,3,*]

SUMMARY

We investigated the role of the N-terminus (residues 1–43) of the myosin essential light chain (N-ELC) in regulating cardiac function in hypertrophic (HCM-A57G) and restrictive (RCM-E143K) cardiomyopathy mice. Both models were cross-genotyped with N-ELC-truncated Δ43 mice, and the offspring were studied using echocardiography and muscle contractile mechanics. In A57G×Δ43 mice, Δ43 expression improved heart function and reduced hypertrophy and fibrosis. No improvements were seen in E143K×Δ43 compared to RCM-E143K mice. HCM-mutant pathology involved an impaired N-ELC tension sensor, disrupted N-ELC-actin interactions, an altered force-pCa relationship, and a destabilized myosin's super-relaxed state. Removal of the malfunctioning N-ELC sensor led to functional rescue in HCM-truncated mutant hearts. However, the RCM mutation could not be rescued by N-ELC deletion, likely due to its proximity to the myosin motor domain, affecting lever-arm rigidity and myosin function. This study provides insights into the role of N-ELC in the development and potential rescue of ELC-mutant cardiomyopathy.

INTRODUCTION

Cardiac muscle contraction results from the ATP-coupled interaction between myosin and actin/troponin (Tn)-tropomyosin (Tm) and is regulated by Ca^{2+} ions. Pathological cardiac remodeling due to hypertrophic (HCM) or restrictive (RCM) cardiomyopathy is most commonly triggered by mutations in sarcomeric proteins of the heart, including myosin heavy chain (β-MHC), myosin binding protein C (MyBP-C), titin, actin, Tm, TnT, TnI, TnC, and both myosin regulatory (RLC) and essential light chain (ELC).[1,2] HCM is an autosomal dominant disease characterized by thickening of the left ventricle (LV) wall and interventricular septum (IVS), myofilament disarray, and interstitial fibrosis. It affects about 1 in 200 people and is one of the leading causes of sudden cardiac death (SCD) in young adults.[3,4] RCM is a less common subtype of HCM and is characterized by increased stiffness of the LV wall with no increase in wall thickness and a largely impaired diastolic function.[5,6] Both HCM and RCM result in insufficient blood pumping to the organs and can lead to impaired relaxation and diastolic dysfunction.

An essential question in cardiomyopathy research is how gene mutations in sarcomeric proteins cause cardiac dysfunction and lead to specific clinical phenotypes. The question that we address in this report regards the molecular basis for phenotypic differences between the two mutations in myosin ELC (*MYL3* gene) identified by population studies to cause HCM or RCM.[7–10] The HCM-associated A57G mutation, in which glycine at position 57 replaces alanine in exon 3 of the *MYL3* gene, was identified in two unrelated Korean families and one Japanese patient diagnosed with HCM and exhibiting asymmetric septal hypertrophy, atrial fibrillation, and SCD.[7,8] In transgenic mice expressing the A57G mutation in their hearts, the left ventricular (LV) tissue exhibited specific phenotypic characteristics consistent with hypertrophic cardiomyopathy remodeling. These characteristics included elevated myofilament Ca^{2+} sensitivity of contractile force, heightened stroke work (SW), increased cardiac output (CO), and significant fibrosis.[11,12] We also studied the effects of A57G on the super-relaxed (SRX) state of myosin,[13] considered crucial to the regulation of sarcomere force production and energy utilization in cardiac muscle.[14,15] We found a shift from myosin's SRX to DRX (disordered relaxed) state in A57G fibers that most likely contributed to hypercontractile myosin behavior and pathological cardiac remodeling in transgenic (Tg) A57G mice.[13]

On the other hand, the RCM-E143K mutation, in which a lysine replaces glutamic acid at position 143, located in exon 4, was identified in a patient admitted for DNA screening following the premature death of his two younger siblings.[9] In another E143K mutated patient, a transthoracic echocardiogram revealed severe biatrial enlargement, preserved biventricular systolic function, no LV hypertrophy, and advanced LV diastolic dysfunction.[10] Studies from our laboratory using transgenic E143K mice showed phenotypic characteristics reminiscent of human RCM, including diastolic dysfunction, low SW and CO, fibrosis, and slightly increased myofilament Ca^{2+} sensitivity of force in male E143K

[1]Department of Molecular and Cellular Pharmacology, University of Miami Miller School of Medicine, Miami, FL 33136, USA
[2]These authors contributed equally
[3]Lead contact
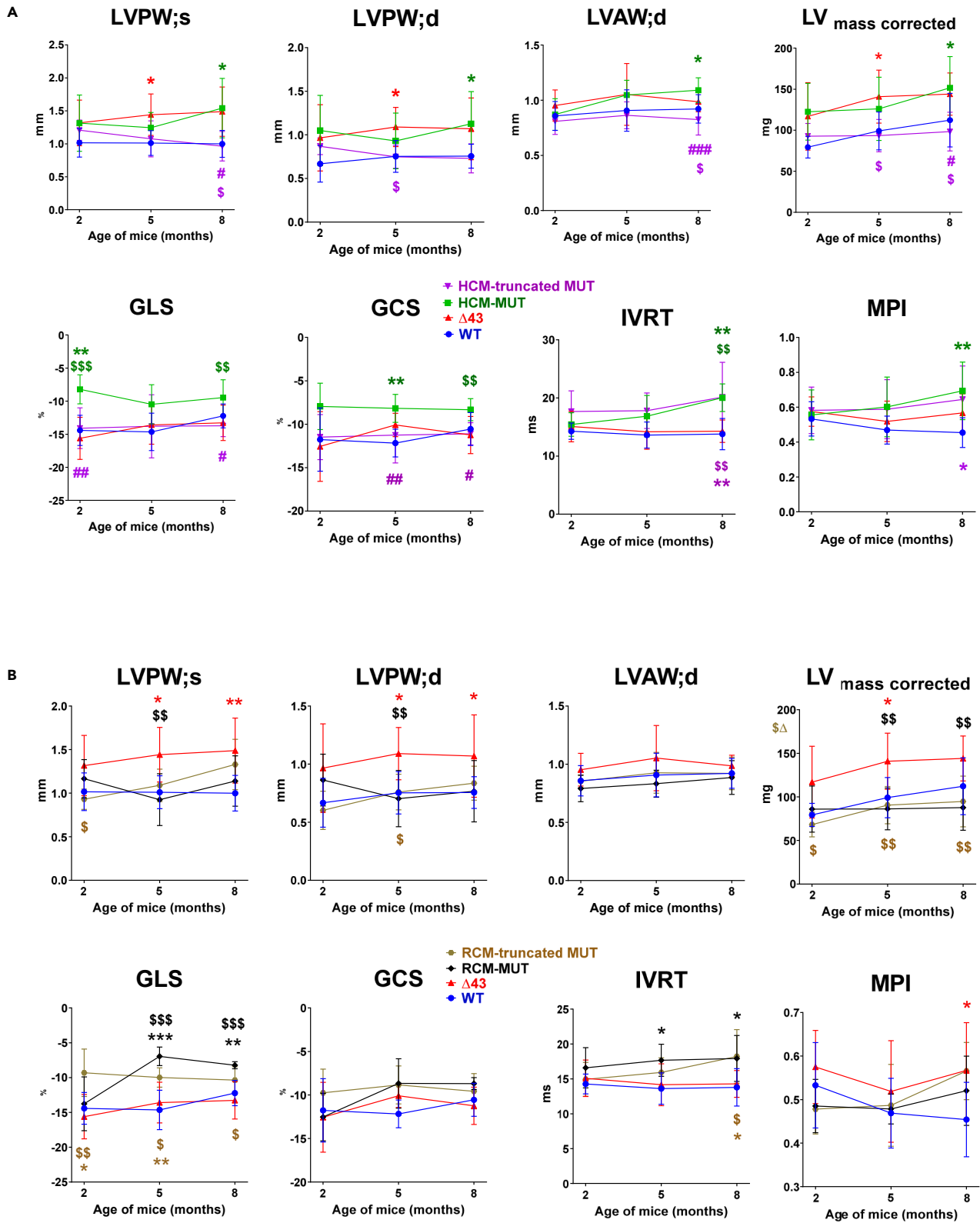*Correspondence: dszczesna@med.miami.edu

Figure 1. Evaluation of heart function in ELC mouse models of cardiomyopathy

Echocardiography measurements were conducted in 2, 5, and 8-month-old WT, Δ43, HCM-mutant, and HCM-truncated mutant mice (A) and WT, Δ43, RCM-mutant, and RCM-truncated mutant mice (B). Parameters measured included LVPW (left ventricular posterior wall thickness in systole and diastole), LVAW (LV anterior wall), and LV mass. Additionally, speckle-tracking-based strain analysis was performed, measuring GLS (global longitudinal strain) and GCS (global circumferential strain). Evaluation of isovolumetric relaxation time (IVRT) and myocardial performance index (MPI) was also conducted. The data represent the mean of n = N° mice (shown in Tables S1–S3) ±SD, with statistical analysis performed using one-way ANOVA with Tukey's multiple comparisons test. Significance is indicated by *p versus WT, $p versus Δ43, and #p versus HCM-mutant.

animals.[16] Interestingly, our recent report by Sitbon et al.[17] showed that RCM-E143K fibers favored the SRX state, suggesting fewer myosin cross-bridges available to participate in cardiac muscle contraction and possibly explaining compromised *in vivo* cardiac function in transgenic E143K mice.[16]

While detrimental phenotypes characterize pathological cardiomyopathy, physiological cardiac hypertrophy can be manifested by an increase in heart size without abnormal morphology, unchanged or enhanced cardiac function,[18] a normal pattern of gene expression,[19] and is usually reversible.[20] Our laboratory generated a mouse model of physiological-like hypertrophy with truncated N-terminus ELC (residues 1–43)[21] that showed hypertrophic cardiac growth with no signs of abnormal morphology or function.[12] Specifically, we were interested in the biological significance of the unique N-terminus of cardiac ELC (N-ELC), depicted as a rod-like 91 Å-long extension that can bridge the ELC core of the myosin head with the actin filament,[22] and its role in actin-myosin interactions, force development, and muscle contraction under normal and disease conditions. Biochemically, we showed that ablation of the N-ELC in Tg-Δ43 mice stabilized the low-energy SRX state,[13] a trend also favored by the RCM-E143K model.[17] At the single-molecule level, we demonstrated that the N-ELC could modulate myosin step size and step frequency, and its deletion led to an increase in 5 nm step frequency with a coincidental loss of the 8 nm step compared to ELC WT myosin.[23,24] We also observed that the lack of N-ELC blunted a sarcomere length-mediated increase in myofilament Ca^{2+} sensitivity, suggesting that the N-ELC of cardiac myosin plays a role in mediating the sarcomere length dependency of cross-bridge detachment kinetics and myofilament Ca^{2+} sensitivity.[25]

In this study, we aimed to investigate whether the deletion of N-ELC could serve as a therapeutic approach to reverse pathological phenotypes associated with HCM-A57G (HCM-mutant) and RCM-E143K (RCM-mutant) ELC variants. We sought to determine if this approach would be effective for both cardiomyopathy ELC mutations or solely for the hypercontractile HCM-A57G mutation, as we suspected. We generated double-mutant animals by crossbreeding HCM/RCM-mutant models with Δ43 mice. Our findings revealed that partial ablation of N-ELC and the introduction of Δ43 in cross-genotype A57G×Δ43 (HCM-truncated) mutant mice reversed cardiac hypertrophy and fibrosis observed in HCM-mutant hearts, restored key factors of intact heart function, and reinstated the disrupted SRX state. In contrast, E143K×Δ43 (RCM-truncated) mutant animals showed no improvements in heart morphology or function compared to RCM-mutant alone and did not prevent fibrotic remodeling.

I-TASSER analysis of single-mutant ELC proteins revealed the presence of an α-helical structure at the N-terminus of ELC in the HCM-A57G mutant, which was absent in the RCM-E143K mutant. The spatial orientation of N-ELC in the RCM mutant was similar to that in WT ELC. These differing structural features in the N-ELC termini of both cardiomyopathy variants, along with the distinct locations of the cardiomyopathy mutations in the ELC molecule, are speculated to be responsible for the phenotypic differences between HCM and RCM mutations, as well as the lack of *in vivo* response in the RCM-truncated mutant model to partial N-ELC deletion.

RESULTS

Generation of cross-genotype A57G×Δ43 (HCM-truncated) and E143K×Δ43 (RCM-truncated) mutants

Our previous findings indicated that N-ELC-truncated (residues 1–43) Δ43 hearts exhibited characteristics resembling physiological-like hypertrophy, with no signs of abnormal morphology or function.[12] To investigate whether the partial removal of the 43-amino acid N-terminus of the myosin essential light chain (N-ELC), in combination with HCM or RCM mutations, could serve as an approach to ameliorate cardiomyopathy in mice, we crossed Δ43 mice with HCM or RCM mutant strains. Offspring positive for the Δ43 and A57G mutations in HCM-truncated mice and Δ43 and E143K in RCM-truncated animals were characterized for transcript and protein expression (Figures S1A–S1D). The results demonstrated that both cross-genotype animal models expressed the following levels of human ventricular ELC mutant proteins (%): 66 ± 9.5 (A57G) and 9 ± 5 (Δ43) in HCM-truncated mutant animals (n = 7 mice), and 55 ± 9.8 (E143K) and 12 ± 4.8 (Δ43) in RCM-truncated mice (n = 6 mice) (Figure S1D). The remaining endogenous mouse ventricular ELC was 25 ± 6% in HCM-truncated and 39 ± 7% in RCM-truncated mutants.

Partial rescue of heart morphology and function in HCM-truncated but not RCM-truncated mutant mice through N-ELC removal

We aimed to assess the impact of partial N-ELC deletion and the introduction of Δ43 on heart morphology and function in double HCM-truncated and RCM-truncated mutant mice compared to HCM/RCM single mutants. Echocardiography evaluations were conducted in all genotypes at 2, 5, and 8 months of age (Figure 1).

At approximately 2 months of age, echocardiography examinations of HCM/RCM-truncated mutant mice revealed no abnormal morphology or differences in ejection fraction (EF), fractional shortening (FS), or E/e' (E = early diastolic mitral inflow velocity/e' = early diastolic mitral annulus velocity) ratios, suggesting normal systolic and diastolic function between double mutant animals compared single

mutant mice, as well as WT and Δ43 mice (Figures 1A and 1B, Table S1). However, an assessment of heart function using speckle-tracking analysis revealed significant impairment in global longitudinal strain (GLS), a metric for left ventricular (LV) strain and deformation, in HCM-mutant compared to WT and Δ43 mice. Notably, GLS was significantly improved in HCM-truncated mutant mice compared to HCM-mutant mice, with GLS values increasing from −8.2 ± 2.2 (HCM-mutant) to −14.1 ± 3.1 in HCM-truncated mutant mice (Figure 1A; Table S1). Since GLS analysis is highly regarded for its effectiveness in detecting subtle changes in myocardial function,[26,27] this result suggested that the presence of Δ43 in the hearts of HCM-truncated mutant animals mitigated heart dysfunction compared with HCM-mutant hearts. In the RCM group, differences were seen between Δ43 and RCM-truncated mutant mice in LVmass and LVPW;s showing lower values for cross-genotype mice (Figure 1B; Table S1). GLS measurements in RCM-truncated mutant mice indicated worsened function compared to RCM-mutant, WT, or Δ43 animals (Figure 1B). Thus, the partial removal of N-ELC ameliorated abnormal sarcomere shortening in 2-month-old HCM-mutant hearts, but not in RCM-mutant mice (Figures 1A and 1B).

In 5-month-old animals, significant reductions in LV posterior wall thickness in diastole and LV mass were observed in HCM-truncated mutants compared to HCM-mutant hearts (Figure 1A; Table S2), suggesting a Δ43-induced recovery in cardiac hypertrophy. No changes in heart morphology were observed in animals of the RCM group (Figure 1B; Table S2). A notable impairment in global circumferential strain was observed in HCM-mutant mice (−8.2 ± 1.6), in comparison to age-matched WT mice (−12.2 ± 1.6), suggesting an HCM-mutant-dependent downregulation of heart performance. This impairment was subsequently mitigated by the partial depletion of N-ELC in HCM-truncated mutant mice (−11.3 ± 3.2) (Figure 1A). Additionally, a significant decline in global longitudinal strain (GLS) was noted in 5-month-old RCM-mutant mice (−7.0 ± 1.3), compared to WT (−14.6 ± 2.8) or Δ43 (−13.6 ± 2.9) animals (Figure 1B), suggesting reduced LV shortening in RCM-mutant animals. Although GLS showed a slight improvement in the hearts of RCM-truncated mutant mice (−10 ± 1.4), the values did not reach the levels observed in WT or Δ43 mice (Figure 1B; Table S2).

Morphological and functional studies of 8-month-old animals showed statistical differences among WT, Δ43, HCM-mutant, and HCM-truncated mutant animals, but no noticeable distinctions were observed between the WT, Δ43, RCM-mutant, and RCM-truncated mutant mice (Figures 1A and 1B, Table S3). In agreement with prior research,[13] we observed significant increases in LV posterior wall thickness in systole (LVPW;s) and diastole (LVPW;d), as well as LV anterior wall thickness in diastole (LVAW;d), along with increased LV mass in HCM-mutant mice compared to WT (Figure 1A), indicating cardiac hypertrophy in 8 month-old HCM mice. LV wall thickness and LV mass values returned to WT levels upon partial deletion of N-ELC and the presence of the Δ43 moiety in HCM-truncated mutant hearts (Figure 1A; Table S3). The beneficial effect of Δ43 expression in HCM-truncated hearts was also evident in the recovery of abnormal GLS and GCS in 8-month-old HCM-truncated mutant mice compared with HCM-mutant littermates (Figure 1A). Morphometric parameters for 8-month-old Δ43 mice closely resembled those of HCM-mutant hearts; however, GLS and GCS remained unaffected, suggesting a normal function in the Δ43 model of nearly physiological hypertrophy (Figure 1A). These findings align with previous reports on Δ43 mice, which depicted hypertrophy of a non-pathological nature in Δ43 mice older than 7 months.[12,21,28]

While hypertrophy and muscle shortening parameters improved upon N-ELC ablation in HCM-truncated mutant animals, the relaxation function remained unaltered (Figure 1A; Tables S1–S3). Pulse-wave and tissue-doppler imaging (TDI) exhibited a persistent lack of recovery in abnormal isovolumetric relaxation time (IVRT) and myocardial performance index (MPI) in HCM-truncated mutant mice when compared to HCM-mutant mice (Figure 1A). This implies that the partial elimination of N-ELC in HCM mice is advantageous in restoring only specific aspects (i.e., LV shortening) of heart function that are compromised in these animals. Much like what was observed in 2-month and 5-month-old RCM mice, no discernible changes in morphology or function upon N-ELC removal were evident in 8-month-old RCM-truncated mutant mice (Figure 1B; Table S3).

Alleviation of cardiac fibrosis in ∼8-month-old HCM-truncated but not RCM-truncated mutant mice

Fibrosis is a maladaptive process occurring in both RCM and HCM patients, and previous findings in RCM-E143K and HCM-A57G mice confirm the occurrence of similar fibrotic remodeling.[11,12,16] In contrast, no fibrosis was seen in the nearly physiological Δ43 model mice.[12,21] In this report, we aimed to investigate whether deleting N-ELC could serve as a therapeutic approach to reverse the fibrotic remodeling associated with the HCM-mutant and RCM-mutant ELC variants and to determine if this strategy would be effective for both mutations or only the hypercontractile HCM mutation.

As previously reported,[11,12] quantification of picrosirius red staining indicated a significantly higher fibrotic content in the LVs of 8-month-old HCM-mutant mice compared to age-matched WT animals, while no differences were observed between the left ventricles (LVs) of WT and Δ43 mice (Figures 2A and 2B). Notably, a significant decrease in the percentage of fibrosis was observed in HCM-truncated mutant mice when compared to HCM-mutant alone, suggesting that partial removal of N-ELC and introducing Δ43 in double mutant mice mitigated fibrotic remodeling in HCM-truncated mutant hearts (Figure 2B). Similarly, as observed in our previous study with RCM-mutant animals,[16] LVs of RCM mice displayed an increase in collagen content compared to WT mice (Figure 2A). However, the deletion of N-ELC in RCM-truncated mutant mice did not result in the alleviation of maladaptive fibrotic remodeling observed in RCM-mutant hearts (Figure 2B).

Mitochondrial remodeling in ∼8-month-old HCM-truncated and RCM-truncated mutant mice

The interplay between sarcomeres and mitochondria in heart cells is crucial for LV function and sarcomeric organization. Previously, we reported no overall defects in mitochondrial function or respiration in HCM, RCM, and Δ43 mutant mice compared to WT animals.[17] Here, we investigated whether any changes could be observed in the overall number and size/area of mitochondria in the LVs of HCM-truncated and RCM-truncated mutant mice compared with respective controls using transmission electron microscopy (TEM) (Figure 3). Our focus
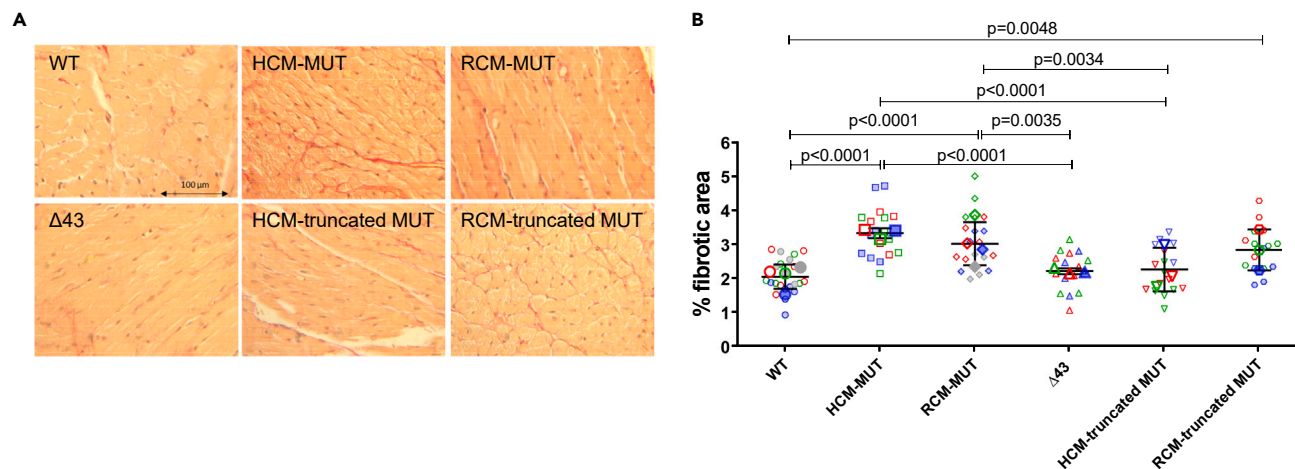
Figure 2. Assessment of fibrosis and collagen content in the left ventricles (LV) of ~8-month-old WT, HCM, RCM, Δ43, HCM-truncated, and RCM-truncated mutant mice

(A) Representative images of picrosirius red-stained LV in mice. Scale bar, 100 μm.

(B) SuperPlots showing the percentage of fibrotic area quantified from a total of 4 WT (2 F and 2 M), 3 HCM-mutant (2 F and 1 M), 4 RCM-mutant (2 F and 2 M), 3 Δ43 (2 F and 1 M), 3 HCM-truncated (3 F), and 3 RCM-truncated (2 F and 1 M) mutant mice. This analysis includes 4–7 LV images per animal and 16–22 per group. The data per animal are presented using large, color-coded symbols (circles for WT, squares for HCM-mutant, diamonds for RCM-mutant, triangles for Δ43, inverse triangles for HCM-truncated, and hexagons for RCM-truncated mutant hearts). The respective image measurements are indicated by small, color-coded symbols. Open symbols indicate female (F), and closed symbols indicate male (M) mice. Data are presented as the mean of n = N° images ±SD (standard deviation), with significance calculated using one-way ANOVA with Tukey's multiple comparisons test.

centered on examining the interplay between sarcomeres and mitochondria within the LVs of mice, a relationship critical for the heart's function in pumping oxygenated blood throughout the body. Representative TEM images at 3000x and 5000× magnification of LV samples from WT, HCM-mutant, RCM-mutant, Δ43, HCM-truncated, and RCM-truncated mutant mice are displayed in Figure 3A. Among WT and Δ43 mice, no differences were observed in the overall sarcomeric structure, with most myofibers showing aligned myofibrils along the long axis of the sarcomeres and the Z disks in register throughout the length of the myofibers. However, visible disruption of sarcomeric organization was observed in the hearts of HCM and RCM cardiomyopathy models (Figure 3A).

The number of mitochondria was found to be highest in RCM-mutant mice (Figure 3B). Consistent with this finding, previous TEM reports identified sarcomere irregularities in 11-month-old RCM-mutant mice compared to WT controls; however, no analysis of overall mitochondrial number/size was conducted.[16] Notably, proteomic analysis of RCM-mutant heart samples revealed significant changes in metabolic processes associated with ATP production and alterations in the expression of energy-related mitochondrial proteins.[16] In comparison to WT samples, both RCM-mutant and RCM-truncated mutant animals demonstrated a markedly higher number of mitochondria (Figure 3B). Nevertheless, when considering the mitochondrial cross-sectional area, no disparities were observed among these genotypes, WT and Δ43 mice (Figure 3C). These findings suggest that the hearts of RCM-mutant mice may accumulate a higher number of possibly smaller mitochondria, and the deletion of N-ELC does not appear to influence this process.

The hearts of HCM-mutant mice were found to have a lower mitochondrial count compared to RCM-mutant and RCM-truncated mutant animals (Figure 3B). Additionally, the mitochondrial cross-sectional area in HCM-mutant mice was significantly smaller than in RCM-mutant samples (Figure 3C). However, the deletion of N-ELC significantly increased the mitochondrial area in HCM-truncated mutant compared with HCM-mutant hearts (Figure 3C). This result suggests that N-ELC deletion may counteract the compromised myosin energetic states observed in HCM-mutant mice, thereby enhancing their mitochondrial reserve to support cardiac function (Figure 3C).

Myosin energetic states in ~8-month-old cross-genotype HCM/RCM-truncated mutant models

The heartbeat relies on the interaction between myosin cross-bridges and actin-Tm/Tn, a process that is dependent on both Ca^{2+} and ATP. Myosin, a hexamer, comprises two coiled-coil myosin heavy chains (MHCs) and two sets of light chains, namely the essential light chain (ELC) and regulatory light chain (RLC), which are attached to their respective binding sites on the lever arm domain of the myosin head, known as IQ motifs.[29] Myosin serves as the molecular motor of the heart, converting the energy from ATP hydrolysis into movement and muscle contraction. In a state of relaxation, the myosin heads undergo physiological transitions between the super-relaxed state (SRX), which optimizes energy preservation and the disordered relaxed state (DRX), where heads may form cross-bridges with actin but consume more ATP.[14] From a structural perspective, it is believed that the SRX heads form an interacting-heads motif (IHM), interacting asymmetrically with each other while folding back onto the myosin backbone.[30–33] In the DRX state, myosin heads extend into the space between filaments, assuming various conformations, some of which are readily available for interaction with actin and the generation of force.[34]
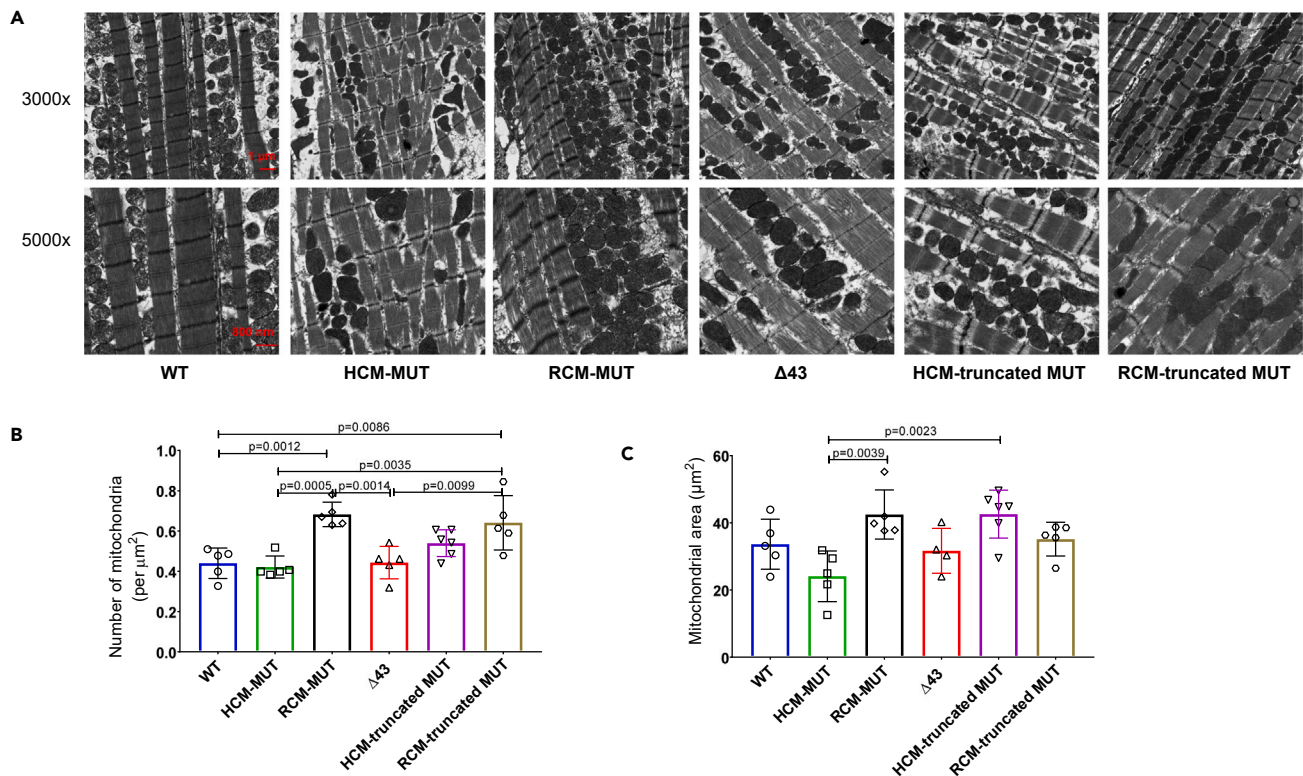
Figure 3. TEM images of LV samples from ~8-month-old female ELC mutant mice

(A) Representative images at 3000x and 5000× magnification of LV samples from WT, HCM-mutant, RCM-mutant, Δ43, HCM-truncated mutant, and RCM-truncated mutant mice. Scale bars, 1 μm (3000x) and 800 nm (5000x).

(B) Number of mitochondria per μm^2 in WT, HCM-mutant, RCM-mutant, Δ43, HCM-truncated mutant, and RCM-truncated mutant hearts analyzed using 3000x images (5 images per animal). Note the significantly increased number of mitochondria in RCM-mutant versus WT, HCM-mutant, and Δ43 mice.

(C) Mitochondrial cross-section area (in μm^2) for the group of mice depicted in B. Note the increased mitochondrial area in HCM-truncated mutant versus HCM-mutant hearts. Data are mean of n = N° images ±SD and analyzed using one-way ANOVA with Tukey's multiple comparisons test.

In the subsequent series of experiments, our objective was to explore the influence of N-ELC deletion on the stability of the SRX state and the biochemical equilibrium between SRX and DRX states in skinned LV papillary muscle (LVPM) fibers sourced from HCM/RCM-truncated mutant hearts. The results were compared to those obtained from previously characterized single mutant mice carrying HCM, RCM, and Δ43 mutations.[13,17] We conducted mant-ATP chase assays on chemically skinned LVPM fibers using the IonOptix instrumentation (IonOptix, LLC), following the protocol outlined in Yuan et al.[35] The fibers were incubated in a rigor solution containing 250 μM mantATP, and after 3-5 min to reach a stable fluorescence level, the fibers were chased with 4 mM non-labeled ATP. Fluorescence decay curves were collected, plotted as a function of time, and fitted to a double-exponential equation: F = 1 – P1 (1 – exp(-t/T1)) – P2 (1 – exp (-t/T2)), where P1 and P2 (%) represent the amplitudes of the fast and slow phases of fluorescence intensity decay, and T1 and T2 are their respective lifetimes (seconds).[13,36] P1 and T1 denote the initial rapid decay in fluorescence intensity, corresponding to myosin in the DRX state and the release of nonspecifically bound mant-ATP, assumed to be fast as well. P2 and T2 represent the slower decrease in fluorescence intensity attributed to myosin in the SRX state.[14] The data were corrected by 0.44 ± 0.02, denoting the fraction of fast-dissociating and nonspecifically bound mant-ATP.[35] The percentage of the SRX state was then calculated as P2/(1–0.44)*100%, and the DRX state as 100-SRX%.[35] As a result of implementing this adjustment, the values for SRX/DRX ratios in single HCM, RCM, and Δ43 mutants reported here (Figure 4) differ from those published previously, where the correction was not applied.[13,17]

Fibers obtained from HCM-mutant mice exhibited a significantly higher proportion of myosin cross-bridges in the DRX state compared to those from WT and Δ43 mice, as depicted in Figure 4A. This observation implies that the A57G mutation destabilized the SRX state, resulting in an increased population of liberated myosin heads—a potential mechanism contributing to hypercontractility (Figure 4A). Intriguingly, the SRX state recovered in HCM-truncated mutant fibers, approaching values similar to those observed in WT and Δ43 mice (Figure 4A). These findings indicate that the expression of Δ43 moiety in HCM-truncated mutant fibers led to the restoration of the SRX state, thereby preventing pathological myosin motor function and abnormal heart contractility, as illustrated in Figure 1A.

Mant-ATP chase experiments conducted on LVPM fibers from WT, RCM-mutat, Δ43, and RCM-truncated mutant mice revealed a significant increase in the percentage of SRX state in RCM-mutant when compared to WT fibers (Figure 4B). This result indicates that, similar to Δ43, the RCM-mutant model tends to favor the sequestered SRX state and aligns with previously published mant-ATP data on RCM-mutant mice.[17]
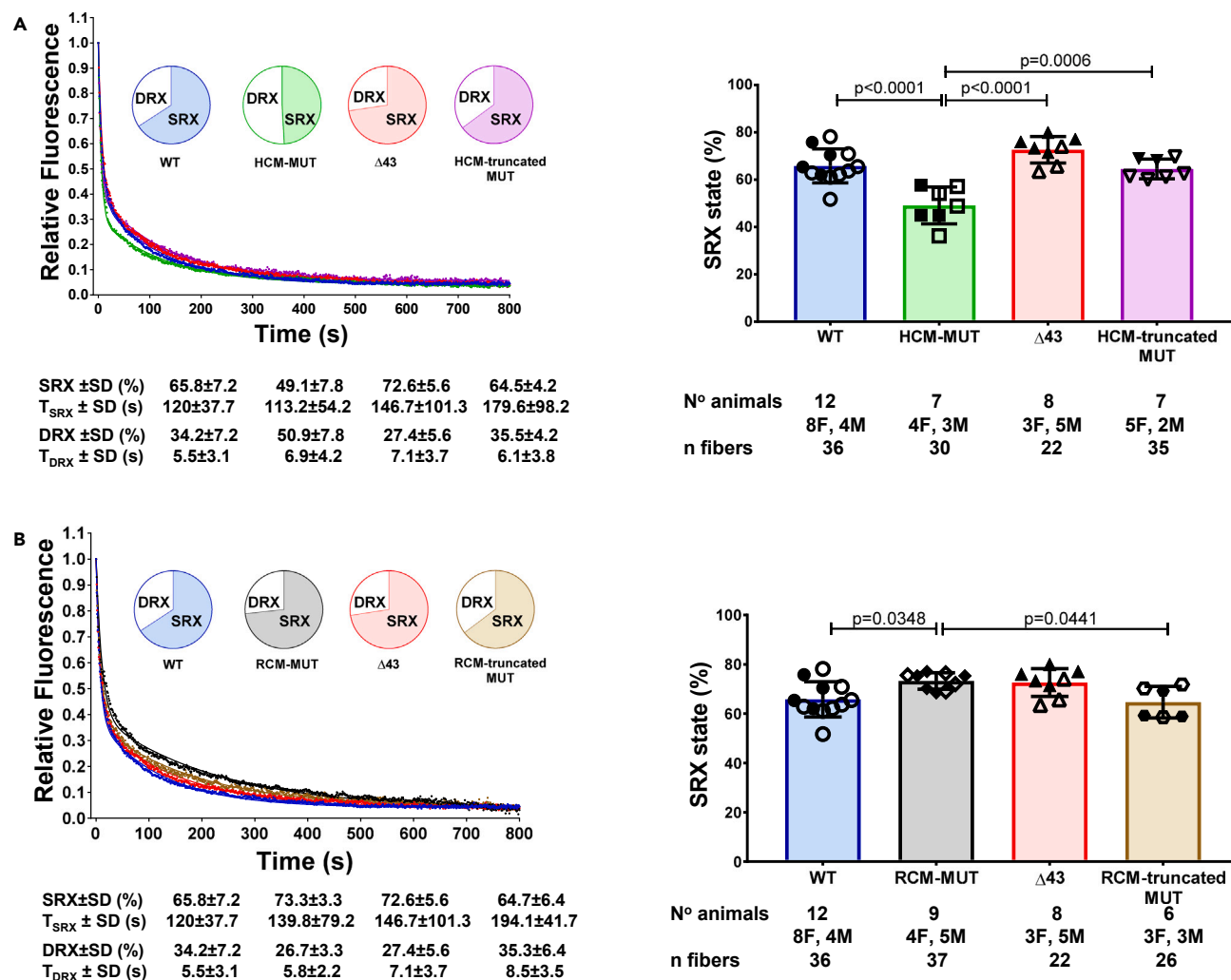
Figure 4. Partial deletion of N-ELC rescues the SRX↔DRX equilibrium in ~8-month-old cross-genotype models

(A and B) HCM-truncated mutant and B. RCM-truncated mutant mice. Values are means of n = N° mice ±SD with significance (p) determined using one-way ANOVA with Tukey's multiple comparisons test. Open symbols represent female mice, and closed symbols represent male mice.

Notably, the SRX/DRX ratio observed for RCM-truncated mutant fibers returned to levels seen in WT ELC mice, which were significantly lower than those observed in the RCM-mutant model (Figure 4B). This outcome suggests that partial deletion of N-ELC can be beneficial in restoring the abnormal SRX↔DRX balance observed in RCM-mutant mice. The same conclusion applies to the N-ELC-deleted HCM mice, indicating that the energetic state of myosin in both HCM and RCM cardiomyopathy models can be restored to WT levels through manipulation of the N-terminus ELC. There were no statistically significant differences in the lifetimes of the fast (T_{DRX}) and slow (T_{SRX}) phases of fluorescence decay between the genotypes (Figure 4).

Regarding our SRX study, a recent paper has raised concerns about the mant-ATP displacement assay, arguing that it may not be suitable for characterizing and quantifying the SRX population of myosin heads.[37] Although the authors demonstrated that mant-ATP decay curves could be successfully fitted with a single exponential for purified myosin subfragments utilized in their investigation, it is crucial to note that such a single exponential fit was found to be inaccurate and inappropriate for quantifying the percentage of the SRX state in skinned muscle fibers presented in the current report. In addition, we verified mant-ATP chase assays performed on LVPM fibers from all genotypes by conducting myofibrillar (MF) ATPase activity assays under calcium-free conditions (Figure S2). The results of MF ATPase assays were consistent with those of the mant-ATP assays. For the HCM-mutant group, the expression of the Δ43 moiety in the HCM-truncated mutant model lowered the basal MF activity compared to the HCM-mutant alone. This is in agreement with the decrease in the percentage of the DRX state in HCM-truncated mutant hearts (Figure 4A).

In summary, the mant-ATP results provided insight into the SRX state, a low-ATPase kinetic state thought to play a cardioprotective role in the hearts of mice. However, the kinetic SRX↔DRX equilibrium may not represent the structural equilibrium between SRX and DRX states. The structural SRX-DRX transition involves the physical conformations of the myosin heads as visualized by cryo-EM[32] or small-angle X-ray
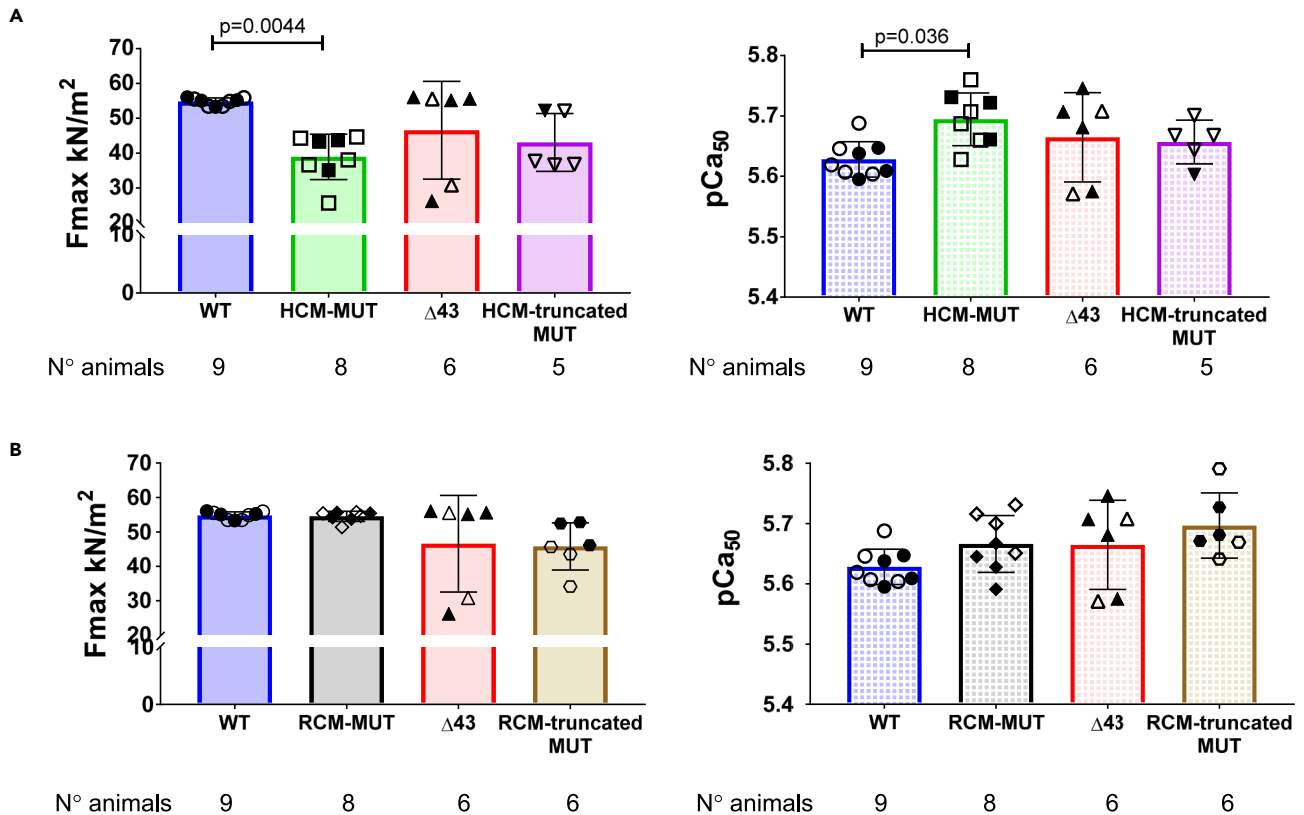
Figure 5. Assessment of contractile function in ELC mouse models of cardiomyopathy

Isometric steady-state force and force-pCa relationship were conducted in LVPM fibers from ~8-month-old WT, HCM-mutant, Δ43, and HCM-truncated mutant (A) and WT, RCM-mutant, Δ43, and RCM-truncated mutant (B) groups. The left panels illustrate maximal tension at pCa4, while the right panels depict the Ca^{2+} sensitivity of force development. The data are presented as means ± SD of n = N° animals (5–10 fibers per heart). Statistical significance was determined using one-way ANOVA with Tukey's multiple comparisons test. Open symbols represent female mice, and closed symbols represent male mice.

diffraction.[38] After applying an important correction for non-specifically bound mant-ATP in LVPM fibers (see STAR Methods), we believe we are measuring the population of slowly cycling myosin heads in the SRX state, which can be interrupted by various conditions including genetic mutations associated with HCM.

Restoration of contractile function in ~8-month-old HCM-truncated mutant mice through N-ELC deletion

The impact of N-ELC removal in cardiomyopathy mouse models on maximal pCa 4 steady-state force and the force-pCa relationship in skinned LVPM fibers from mice is illustrated in Figure 5 and detailed in Table S4. As previously reported,[11] F_{max} in LVPM fibers from HCM-mutant mice (38.9 ± 6.5 kN/m^2) was significantly lower than in WT-ELC (54.8 ± 1.1). However, the expression of Δ43 moiety in HCM-truncated mutant fibers led to an increase in F_{max} to 43.1 ± 3.7 kN/m^2, eliminating the significant difference compared to WT (Figure 5A; Table S4). Similarly, the calcium sensitivity of force in the HCM-mutant model was significantly higher than in WT, but pCa_{50} measured in HCM-truncated mutant fibers was no different from that of WT or Δ43 fibers (Figure 5A; Table S4). These findings on force development in the HCM-mutant model align with the SRX study results (Figure 4A) and suggest that partial N-ELC removal and incorporation of Δ43 moiety in HCM-truncated mutant hearts may be advantageous in mitigating HCM-induced hypercontractility and improving heart function *in vivo* (Figure 1A). Therefore, the manipulation of N-ELC and the expression of Δ43 in HCM-ELC mice underlie the mechanism of restoring their LV function.

Regarding the steady-state parameters of contraction in LVPM fibers from RCM-truncated mutant hearts, no alterations in cardiac muscle fiber mechanics were observed compared to RCM-mutant mice (Figure 5B; Table S4). This lack of changes upon partial N-ELC deletion in RCM-truncated mutant hearts remains consistent with the findings from the echocardiography study, where no improvement in heart function *in vivo* was noted in RCM-truncated mutant versus RCM-mutant mice (Figures 1B and 4B).

The Hill coefficient (n_H) values for calcium activation align with the *in vivo* phenotypes observed in HCM and RCM mutant models, as assessed by echocardiography and invasive hemodynamics.[11,16] The hypocontractility of the RCM-mutant is reflected by a decreased n_H, while an elevated n_H may indicate the hypercontractility phenotype. The expression of Δ43 in HCM-truncated mutant mice significantly reduced n_H compared with HCM-mutant mice, mitigating the hypercontractility phenotype. In contrast, the presence of Δ43 in RCM-truncated mutant mice did not rescue the low n_H and no difference in n_H was observed between RCM-mutant and RCM-truncated mutant hearts (Table S4).

A

UREA PAGE

RLC
+P-RLC

WT / WT / HCM-MUT / Δ43 / HCM-truncated MUT / RCM-MUT / RCM-truncated MUT / +P WT RLC std. / -P WT RLC std.
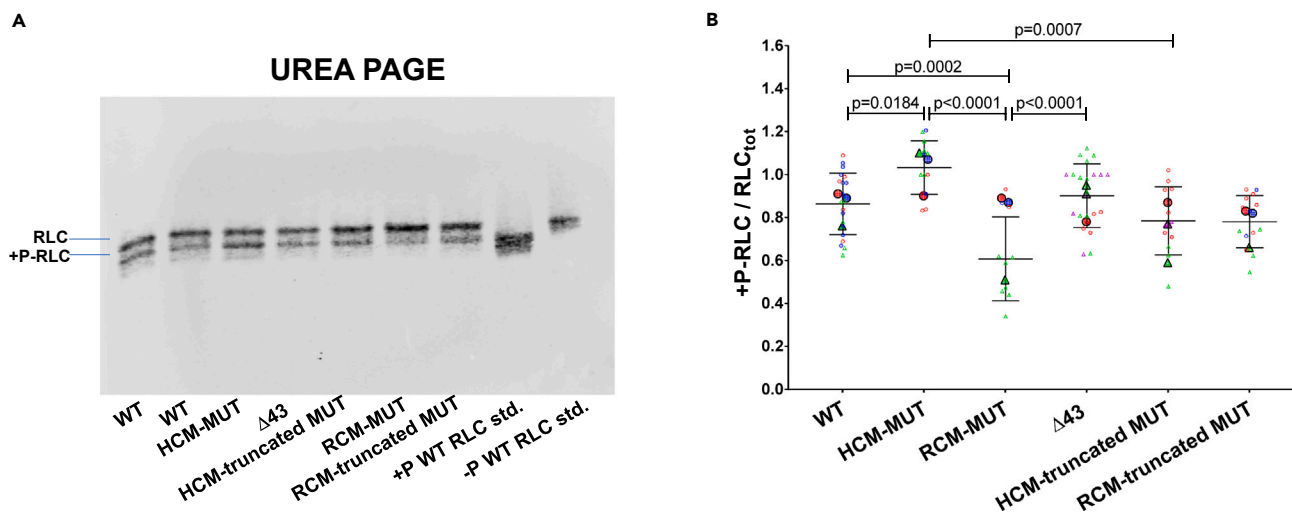
B

Figure 6. Effect of N-ELC deletion on myosin RLC phosphorylation in ∼8-month-old double ELC mutant mice

(A) Representative western blot of 8 M urea extracts from left ventricle (LV) samples separated by urea-PAGE. Phosphorylated (+P-RLC) and non-phosphorylated forms of RLC were separated based on differences in their isoelectric points (pI) and detected using a myosin RLC-specific antibody (CT-1) developed in our laboratory.

(B) Quantification of myosin RLC phosphorylation in the hearts of WT, HCM-mutant, RCM-mutant, Δ43, HCM-truncated mutant, and RCM-truncated mutant mice, represented as SuperPlots. Data for each animal (three animals per group) are depicted using large, color-coded symbols, with triangles representing male mice and circles depicting female mice. Individual mouse measurements are indicated by small, color-coded symbols, with error bars denoting standard deviations. Data are presented as the mean of n = Nº animals ±SD with significance calculated using one-way ANOVA with Tukey's multiple comparisons test.

It is worth mentioning that the published values of the Hill coefficient for the HCM-mutant[11] and RCM-mutant[16] models align with those established in this study.

Normalization of myosin RLC phosphorylation in ∼8-month-old cross-genotype mice

The phosphorylation of myosin RLC by cardiac myosin light-chain kinase (cMLCK) plays a crucial role in regulating heart contraction, both in health and disease.[39,40] Our recent findings have demonstrated that RLC phosphorylation levels are elevated in HCM-mutant hearts and reduced in RCM-mutant hearts compared to WT ELC.[17] These results were corroborated in the present study, where increased levels of RLC phosphorylation were observed in LV samples of HCM-mutant mice compared to WT mice, while decreased levels were observed in RCM-mutant preparations (Figure 6). Figure 6A displays a representative western blot of 8 M urea extracts from LV samples subjected to urea-PAGE, illustrating the separation of phosphorylated and non-phosphorylated forms of RLC, which were detected using a myosin RLC-specific antibody. The quantification of myosin RLC phosphorylation in WT, HCM-mutant, RCM-mutant, Δ43, HCM-truncated mutant, and RCM-truncated mutant mice is presented in the form of SuperPlots[41] in Figure 6B. To determine the average RLC phosphorylation in these mice, data from three animals per group were analyzed. The bands corresponding to phosphorylated and non-phosphorylated forms of RLC were separated based on the differing isoelectric points (pI) of the respective proteins and were detected using the myosin RLC-specific antibody (Figure 6A). Notably, these findings regarding myosin RLC phosphorylation, both from previous and current studies, corresponded with the observed increases and decreases in the DRX state in HCM-mutant and RCM-mutant hearts, respectively (Figure 4).

The partial deletion of the N-terminus ELC was observed to standardize myosin RLC phosphorylation in both HCM/RCM-truncated mutant mice, with levels of RLC phosphorylation not differing significantly from those in WT hearts (Figure 6B). The decrease in myosin RLC phosphorylation in HCM-truncated versus HCM-mutant mice may account for the respective decrease in the DRX state in these hearts (Figure 4A), thereby restoring the SRX/DRX equilibrium to the level observed for WT hearts.

Differential impact of HCM and RCM mutations on N-ELC conformation

Given the previously reported phenotypic disparities between HCM-mutant and RCM-mutant mice[17] and the functional distinctions observed between HCM-truncated and RCM-truncated double-crosses in this study, we sought to investigate whether these variations could be attributed to different effects of the A57G and E143K mutations on the conformation of the N-terminus ELC (Figure 7). Because high-resolution structures of the N-ELC are absent from recent cryo-electron microscopy (cryo-EM) studies on human cardiac myosin,[32] as well as cryo-electron tomography (cryo-ET) investigations of the relaxed cardiac sarcomere,[42] we utilized I-TASSER to compute the structure of the human ventricular WT, Δ43, A57G, and E143K, using protein templates sourced from the Protein DataBank library (Figure 7). The full-length protein was reconstructed from the excised fragments and modeled into the lowest energy conformation, after which the predicted ELC mutant structures were visualized using PyMOL (www.pymol.org).
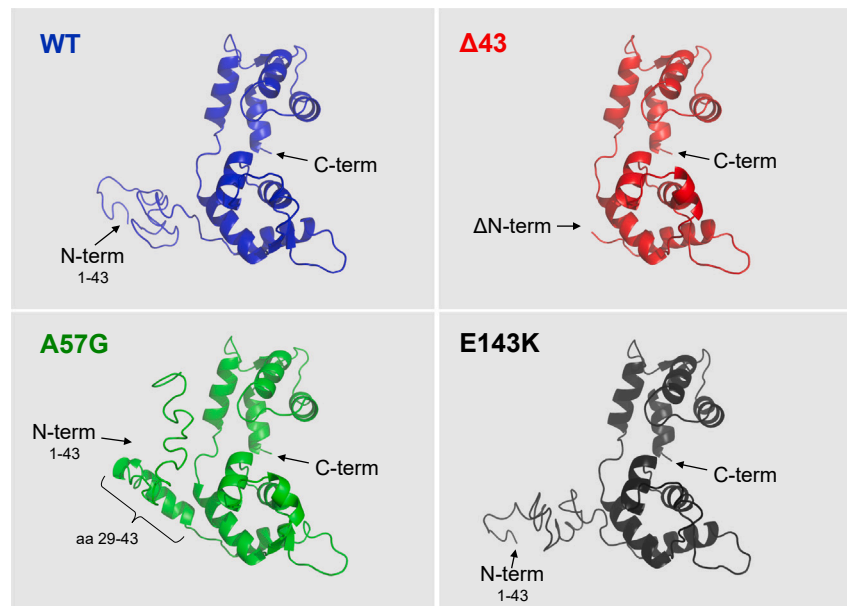
Figure 7. I-TASSER modeled structures of the human ventricular WT, Δ43, A57G, and E143K ELC mutants
Notably, the A57G mutation leads to changes in the spatial arrangement of the N-terminus when compared to the WT and the E143K mutant. These changes are likely attributed to the presence of a helical structure(s) between amino acids 29–43 in A57G-ELC, which is not observed in the WT or E143K.

The most significant difference was observed in the spatial positioning of the N-terminus of ELC in the HCM-mutant compared to WT-ELC (Figure 7). Conversely, the N-terminus of the RCM-mutant assumed a position similar to that of the WT, with no apparent structural disparities between these two molecules (Figure 7). Further analysis using I-TASSER on A57G revealed the presence of an α-helical region within its N-terminus, spanning amino acids 29–43. This structural feature was absent in the N-termini of both WT and E143K proteins (Figure 7). The 43-amino acid long N-ELC of both WT and E143K proteins formed an unfolded coil structure, rendering it distinctly different from the N-terminus of A57G (Figure 7).

Previous low-angle X-ray diffraction studies on LVPM fibers in rigor revealed a decreased interfilament lattice spacing in the A57G myocardium compared with WT-ELC fibers.[12] The findings of the current study reinforce our prior research and propose that the presence of an α-helical structure in the N-ELC of HCM-mutant myocardium could intensify the interaction between myosin and thin filaments under low calcium concentrations, thereby destabilizing the SRX state of myosin (Figure 4). This phenomenon is associated with a hypercontractility phenotype (Figure 5) and might contribute to the observed alterations in heart performance in HCM-mutant mice[11] (Figure 1).

Through partial deletion of the N-ELC and introduction of Δ43 in HCM-truncated mutant hearts led to the restoration of function both *in vivo* (Figure 1) and *in vitro* (Figures 4 and 5). Likely, the partial removal of α-helical hindrance in the N-ELC of the HCM-mutant allows it to function similarly to Δ43 and/or WT proteins. Consequently, this structural realignment at the molecular level facilitates the rescue of function in HCM-truncated mutant mice (Figures 1, 2, 3, 4, 5, and 6). On the other hand, as there were no discernible differences in the conformation of the N-ELC between RCM-mutant and WT myocardium, the removal of the N-terminus in the RCM-mutant model did not induce significant functional changes at the molecular or *in vivo* level.

DISCUSSION

The results obtained from our investigation on cross-genotype HCM/RCM mouse models provide valuable insights into the crucial role of the cardiac myosin ELC and its N-terminus in myosin motor function, as well as intricate mechanisms underlying cardiomyopathies. Previous characterization of single mutant models using echocardiography revealed increased stroke work, cardiac output, and enhanced cardiac contractility in HCM-mutant mice,[11] whereas reduced heart function was observed in the RCM-mutant model.[16] No significant differences from WT were observed in Δ43 animals. Echocardiography results were consistent with single myosin motor characteristics identified in single-molecule studies, showing an increase in myosin power in HCM mice and a decrease in power in RCM animals. This suggests that myosin motors adapt to changing load demands in correspondence with the *in vivo* system.[24]

In particular, our focus was on investigating the role of the N-ELC in the development of specific cardiomyopathy phenotypes and its potential as a target for therapeutic intervention. Prior NMR studies[43] had indicated the significance of this crucial ELC region, which is characterized by proline-alanine repeats and an array of lysine residues, hinting at its possible involvement in molecular interactions with actin during muscle activation.[22] Our hypothesis revolved around the notion that the N-ELC could act as a strain sensor, potentially competing with the conventional lever arm strain sensor.[24,44] Our single-molecule studies have unveiled that the A57G mutation, located near the N-ELC, exerts its effects by directly modifying the N-ELC-actin interaction, distinguishing it from the E143K mutation, which is closer to the myosin motor

domain and likely alters the interaction dynamics between the ELC and the myosin heavy chain (MHC).[24] Specifically, our super-resolution Qdot *in vitro* motility assay showed that the HCM mutant disrupts the binding of N-ELC to actin and interferes with ATP-induced actin detachment due to impaired tension sensing at the N-terminus. Conversely, the RCM mutation was found to disrupt strain-inhibited ADP release, as indicated by an increased probability of a 5 nm step size under load, attributed to reduced lever arm rigidity.[24] These findings suggest that these two ELC mutations elicit contrasting responses to load and contribute to heart pathology through distinct mechanisms.

Our interest in exploring therapeutic approaches related to the N-terminus ELC was motivated by our earlier studies, which demonstrated that the removal of the N-ELC, encompassing amino acids 1–43 in transgenic Δ43 mice, resulted in non-pathological cardiac remodeling characterized by physiologic-like cardiac growth, normal heart morphology, and function.[12,21] Transgenic Δ43 hearts favored the energy conservation state of myosin and stabilized the SRX state.[13,17] Based on this background, we hypothesized that introducing the Δ43 ELC mutant into hypercontractile HCM-mutant hearts could mitigate the hypercontractility phenotype, prevent or reverse fibrotic remodeling, and normalize the DRX↔SRX equilibrium in HCM-truncated mutant mice.

The current results demonstrate a partial mitigation of the *in vivo* phenotype in HCM-truncated versus HCM-mutant hearts (Figures 1A and 2A), while no rescue due to Δ43 expression was observed in RCM-truncated mutant animals (Figures 1B and 2B). One must ensure that the lower expression of the target A57G mutation in A57G×Δ43 mice, changing from 80 ± 5.6% in HCM-A57G to 66 ± 9.5% in HCM-truncated mutant animals (Figure S1), was not responsible for the improved function observed in HCM-truncated mutant hearts. Our earlier studies showed no differences between the three lines of HCM-A57G mice in contractile measurements, myosin ATPase activity, or kinetics of actomyosin interaction. Additionally, no differences were noted in the *in vivo* echocardiographic assessments of the mice. This lack of differences was observed despite varying transgenic protein expression levels in the A57G mouse lines (L1, L5, and L2, expressing ∼80%, ∼75%, and ∼55% of A57G mutant protein, respectively).[11,12] The HCM-truncated mutant model exhibited Δ43-induced restoration of critical parameters associated with HCM-mutant-related heart dysfunction despite a relatively low expression of Δ43 in the hearts of A57G×Δ43 mice. Specifically, we analyzed the global longitudinal strain (GLS) and global circumferential strain (GCS), both methods recognized for their ability to detect early and subtle changes in LV function.[26,27] HCM-truncated mutant hearts exhibited significantly improved heart function compared to HCM-mutant hearts, as evidenced by more negative values of GLS and GCS (Figure 1A). These findings align with the significant reduction of fibrosis observed in the HCM-truncated mutant myocardium compared to HCM-mutant hearts (Figure 2). Additionally, we observed a Δ43-mediated normalization of the calcium sensitivity of force in HCM-truncated mutant myocardium (Figure 5A; Table S4). One common hypothesis for the cause of HCM is hyperactive myosin behavior, which could be linked to a reduction in the population of SRX cross-bridges. This has led to a search for drugs to stabilize the SRX state.[32,45] The Δ43 moiety achieved this in HCM-truncated mutant hearts. It reduced the percentage of energy-consuming DRX heads and stabilized myosin's SRX state in HCM-truncated mutant hearts (Figure 4A), ultimately resulting in improved function (Figure 1A).

However, the data concerning RCM-truncated mice revealed a somewhat complex mechanism. The partial deletion of the N-ELC proved ineffective in improving cardiac function, and abnormal GLS readings were exacerbated in RCM-truncated mutant hearts (Figure 1B). Results from the echocardiographic evaluation of RCM-mutant and RCM-truncated mutant hearts were consistent with the lack of attenuating fibrosis in the latter, which was significantly increased in RCM-mutant hearts (Figure 2B). In comparison to WT hearts, the RCM-mutant animals demonstrated a significantly higher number of mitochondria (Figure 3B) interspersed between myofibrils, facilitating muscle contraction and actin-myosin interactions with adenosine triphosphate (ATP).[46] This finding corresponds with the RCM-mutant model favoring the sequestered SRX state observed in mant-ATP experiments (Figure 4B). Interestingly, the SRX/DRX ratio returned to levels seen in WT ELC mice upon N-ELC removal in RCM-truncated mutant hearts (Figure 4B). When compared to the RCM-mutant model, the SRX state was notably downregulated in HCM-mutant mice, coinciding with a lower number and area of mitochondria in this model (Figures 3B, 3C, and 4A). Deletion of N-ELC in HCM-truncated mutant hearts resulted in a significant increase in mitochondrial area (Figure 3C) and an increase in SRX in HCM-truncated compared to HCM-mutant hearts (Figure 4A).

There are currently no high-resolution structures available of the N-terminus ELC, which is proposed to interact with actin during cardiac muscle contraction.[22,24] The structure of N-ELC is absent from recent cryo-EM studies on human cardiac myosin,[32,33] which exclude the N-terminal 38 amino acids of the ELC. Additionally, cryo-ET studies determining the molecular architecture of native cardiac sarcomeres in the relaxed state also do not include the N-ELC.[42] This lack of atomic details regarding the N-ELC-actin interaction prompted us to analyze predicted structures of ELC proteins using I-TASSER. The analysis of I-TASSER structures of WT, Δ43, A57G, and E143K ELC proteins, illustrated in Figure 7, revealed the presence of a unique α-helical structure in the N-terminus of the HCM-mutant, resulting in a distinct spatial arrangement compared to the WT or RCM-mutant, both of which lack this structural feature in their N-termini. These differing positions of the N-ELC in the two cardiomyopathy models (Figure 7) likely contribute to the observed functional disparities between HCM-A57G and RCM-E143K mice, as previously documented.[17] One can speculate that the A57G mutation facilitates the movement of the α-helical portion within the N-ELC closer to the thin filaments. This proximity enhances interactions between actin and myosin, resulting in heart hypercontractility and pathologic cardiac remodeling, as observed in HCM-mutant hearts both *in vivo*[11] and *in vitro*.[17,24] The partial removal of the α-helical hindrance within the N-ELC of A57G aligns its behavior more closely with that of Δ43 and/or WT ELC protein. In contrast, since there were no discernible differences in the conformation of the N-ELC in RCM-mutant versus WT, the removal of N-ELC in E143K did not induce similar changes at the molecular or intact heart function levels.

In addition to the ELC-related distinctions, the phosphorylation of myosin RLC showed contrasting patterns in HCM-mutant versus RCM-mutant hearts compared to WT ELC mice (Figure 6), further contributing to the functional disparities between these models. We hypothesize that the differential physiological outcomes observed *in vivo* in both cardiomyopathy hearts were, in part, due to the upregulation of myosin

RLC phosphorylation in the hearts of HCM mice and the downregulation of RLC phosphorylation in RCM animals observed previously[16] and in this study (Figure 6). Interestingly, RLC phosphorylation in HCM-truncated and RCM-truncated mutant models was normalized to the level observed for WT ELC mice (Figure 6). Consequently, the double mutant mice demonstrated an increased percentage of SRX state in HCM-truncated versus HCM-mutant hearts (Figure 4A) and a decreased SRX state in RCM-truncated mutant mice compared to RCM-mutant animals (Figure 4B). Therefore, myosin RLC phosphorylation emerges as a critical factor regulating myosin's energetic states in cardiomyopathic ELC hearts, thereby influencing heart function in *MYL3* mutated animals. Our findings are consistent with the study conducted by Lee et al., which demonstrated that increased myosin RLC phosphorylation in the regulatory subunit of myosin phosphatase (MYPT2) knockout mice directly correlated with an elevation in the number of myosin heads in the DRX state.[47] Additionally, our results corroborate the findings of Hitsumoto et al., who showed that RLC phosphorylation mediates the regulation of the SRX/DRX balance in cardiac myosin light-chain kinase (cMLCK)-activated human induced pluripotent stem cell-derived cardiomyocytes.[48]

In conclusion, our findings illuminate the mechanisms by which missense mutations in cardiac myosin ELC lead to dominant myopathies through distinct molecular pathways, underscoring the complexities of protein-protein interplay within the cardiac sarcomere. Structural disparities in the N-termini of the ELC mutants provided valuable insights into their molecular differences and inspired therapeutic interventions mediated by Δ43 ELC. The therapeutic potential of Δ43 to treat HCM-related hypercontractility of HCM-A57G hearts can be attributed to its ability to shift myosin heads from the DRX state to the SRX state (Figure 4A), thereby reducing ATP consumption and improving cardiac function (Figure 1A). We believe that Δ43 could feasibly serve as a rescue approach for sarcomeric mutations beyond ELC that manifest a hypercontractile phenotype. However, the RCM mutation could not be rescued with the N-ELC deletion. Its close proximity to the myosin motor domain likely influenced the rigidity of the lever arm, as concluded in our single-molecule studies,[24] resulting in compromised myosin function and thus heart performance. Alternative measures, such as increasing myosin RLC phosphorylation, need to be undertaken to mitigate the effects of this RCM mutation.

Limitations of the study

Our study has several limitations. Firstly, due to the consistently low expression of Δ43 in double mutant mice obtained in a series of breeding experiments, we could not investigate the gene dose effect of Δ43 on the recovery of GLS and GCS parameters, reduction of fibrosis, and reinstatement of the SRX state in HCM-truncated mutant mice. Higher expression levels could have provided valuable insights. Furthermore, an insufficient number of mice of both sexes limited our ability to compare potential sex-based differences in response to N-ELC deletion interventions. We also did not explore the causal effect of RLC phosphorylation on rescuing function in RCM-truncated mutant mice, leaving a significant aspect unaddressed. Additionally, we currently lack high-resolution structural information regarding the N-terminus of ELC and its level of disorder. We must also acknowledge the limitations of the I-TASSER software in predicting disordered proteins. This obstacle could be circumvented by future studies aimed at obtaining high-resolution structures of the interaction between N-ELC and actin-containing thin filaments, as well as examining the impact of N-ELC deletion in both healthy hearts and those with hypercontractile HCM mutations. Such studies would provide valuable insights into the precise mechanisms underlying the role of the Δ43 entity in mitigating the HCM-related pathogenic phenotype.

STAR★METHODS

Detailed methods are provided in the online version of this paper and include the following:

- KEY RESOURCES TABLE
- RESOURCE AVAILABILITY
  - Lead contact
  - Materials availability
  - Data and code availability
- EXPERIMENTAL MODEL AND STUDY PARTICIPANT DETAILS
  - Mouse models
  - Transgenic mice
- METHOD DETAILS
  - Determination of transgene and protein expression in double mutant mice
  - Conventional and speckle tracking echocardiography (STE)
  - Pulse-wave (PW) and tissue Doppler imaging (TDI)
  - Morphometric heart analysis
  - Quantification of fibrosis by picrosirius red staining
  - Electron microscopy
  - Steady state maximal force and calcium sensitivity measurements
  - Myofibrillar (MF) ATPase activity assays
  - Mant-ATP chase experiments
  - Assessment of protein phosphorylation
  - Secondary structure prediction
- QUANTIFICATION AND STATISTICAL ANALYSIS

SUPPLEMENTAL INFORMATION

Supplemental information can be found online at https://doi.org/10.1016/j.isci.2024.110591.

AUTHOR CONTRIBUTIONS

Y.H.S., K.K., and D.S-C. conceived and designed the study; Y.H.S., K.K., J.L., and A.J.K. performed experiments; R.K-T. supervised echocardiography in mice. Y.H.S., K.K., and J.V. performed I-TASSER/PyMOL modeling; Y.H.S., K.K., R.K-T., and D.S-C. analyzed the data; Y.H.S., K.K., and D.S-C. wrote the manuscript; D.S-C. edited and wrote the final version of the manuscript.

DECLARATION OF INTERESTS

The authors declare no competing interests.

REFERENCES

1. Alcalai, R., Seidman, J.G., and Seidman, C.E. (2008). Genetic Basis of Hypertrophic Cardiomyopathy: From Bench to the Clinics. J. Cardiovasc. Electrophysiol. *19*, 104–110. https://doi.org/10.1111/j.1540-8167.2007.00965.x.

2. Seidman, C.E., and Seidman, J.G. (2011). Identifying sarcomere gene mutations in hypertrophic cardiomyopathy: a personal history. Circ. Res. *108*, 743–750. https://doi.org/10.1161/CIRCRESAHA.110.223834.

3. Semsarian, C., Ingles, J., Maron, M.S., and Maron, B.J. (2015). New perspectives on the prevalence of hypertrophic cardiomyopathy. J. Am. Coll. Cardiol. *65*, 1249–1254. https://doi.org/10.1016/j.jacc.2015.01.019.

4. Semsarian, C., Ingles, J., and Wilde, A.A.M. (2015). Sudden cardiac death in the young: the molecular autopsy and a practical approach to surviving relatives. Eur. Heart J. *36*, 1290–1296. https://doi.org/10.1093/eurheartj/ehv063.

5. Yadav, S., Sitbon, Y.H., Kazmierczak, K., and Szczesna-Cordary, D. (2019). Hereditary heart disease: pathophysiology, clinical presentation, and animal models of HCM, RCM, and DCM associated with mutations in cardiac myosin light chains. Pflügers Archiv *471*, 683–699. https://doi.org/10.1007/s00424-019-02257-4.

6. Rapezzi, C., Aimo, A., Barison, A., Emdin, M., Porcari, A., Linhart, A., Keren, A., Merlo, M., and Sinagra, G. (2022). Restrictive cardiomyopathy: definition and diagnosis. Eur. Heart J. *43*, 4679–4693. https://doi.org/10.1093/eurheartj/ehac543.

7. Lee, W., Hwang, T.H., Kimura, A., Park, S.W., Satoh, M., Nishi, H., Harada, H., Toyama, J., and Park, J.E. (2001). Different expressivity of a ventricular essential myosin light chain gene Ala57Gly mutation in familial hypertrophic cardiomyopathy. Am. Heart J. *141*, 184–189.

8. Choi, J.O., Yu, C.W., Chun Nah, J., Rang Park, J., Lee, B.S., Jeong Choi, Y., Cho, B.R., Lee, S.C., Woo Park, S., Kimura, A., and Euy Park, J. (2010). Long-term outcome of 4 Korean families with hypertrophic cardiomyopathy caused by 4 different mutations. Clin. Cardiol. *33*, 430–438. https://doi.org/10.1002/clc.20795.

9. Olson, T.M., Karst, M.L., Whitby, F.G., and Driscoll, D.J. (2002). Myosin Light Chain Mutation Causes Autosomal Recessive Cardiomyopathy With Mid-Cavitary Hypertrophy and Restrictive Physiology. Circulation *105*, 2337–2340.

10. Caleshu, C., Sakhuja, R., Nussbaum, R.L., Schiller, N.B., Ursell, P.C., Eng, C., De Marco, T., McGlothlin, D., Burchard, E.G., and Rame, J.E. (2011). Furthering the link between the sarcomere and primary cardiomyopathies: Restrictive cardiomyopathy associated with multiple mutations in genes previously associated with hypertrophic or dilated cardiomyopathy. Am. J. Med. Genet. *155A*, 2229–2235. https://doi.org/10.1002/ajmg.a.34097.

11. Kazmierczak, K., Paulino, E.C., Huang, W., Muthu, P., Liang, J., Yuan, C.C., Rojas, A.I., Hare, J.M., and Szczesna-Cordary, D. (2013). Discrete effects of A57G-myosin essential light chain mutation associated with familial hypertrophic cardiomyopathy. Am. J. Physiol. Heart Circ. Physiol. *305*, H575–H589.

12. Muthu, P., Wang, L., Yuan, C.C., Kazmierczak, K., Huang, W., Hernandez, O.M., Kawai, M., Irving, T.C., and Szczesna-Cordary, D. (2011). Structural and functional aspects of the myosin essential light chain in cardiac muscle contraction. Faseb. J. *25*, 4394–4405. https://doi.org/10.1096/fj.11-191973.

13. Sitbon, Y.H., Kazmierczak, K., Liang, J., Yadav, S., Veerasammy, M., Kanashiro-Takeuchi, R.M., and Szczesna-Cordary, D. (2020). Ablation of the N terminus of cardiac essential light chain promotes the super-relaxed state of myosin and counteracts hypercontractility in hypertrophic cardiomyopathy mutant mice. FEBS J. *287*, 3989–4004. https://doi.org/10.1111/febs.15243.

14. Hooijman, P., Stewart, M.A., and Cooke, R. (2011). A new state of cardiac Myosin with very slow ATP turnover: a potential cardioprotective mechanism in the heart. Biophys. J. *100*, 1969–1976. https://doi.org/10.1016/j.bpj.2011.02.061.

15. Toepfer, C.N., Garfinkel, A.C., Venturini, G., Wakimoto, H., Repetti, G., Alamo, L., Sharma, A., Agarwal, R., Ewoldt, J.K., Cloonan, P., et al. (2020). Myosin Sequestration Regulates Sarcomere Function, Cardiomyocyte Energetics, and Metabolism, Informing the Pathogenesis of Hypertrophic Cardiomyopathy. Circulation *141*, 828–842. https://doi.org/10.1161/CIRCULATIONAHA.119.042339.

16. Yuan, C.C., Kazmierczak, K., Liang, J., Kanashiro-Takeuchi, R., Irving, T.C., Gomes, A.V., Wang, Y., Burghardt, T.P., and Szczesna-Cordary, D. (2017). Hypercontractile mutant of ventricular myosin essential light chain leads to disruption of sarcomeric structure and function and results in restrictive cardiomyopathy in mice. Cardiovasc. Res. *113*, 1124–1136. https://doi.org/10.1093/cvr/cvx060.

17. Sitbon, Y.H., Diaz, F., Kazmierczak, K., Liang, J., Wangpaichitr, M., and Szczesna-Cordary, D. (2021). Cardiomyopathic mutations in essential light chain reveal mechanisms regulating the super relaxed state of myosin. J. Gen. Physiol. *153*, e202012801. https://doi.org/10.1085/jgp.202012801.

18. Gomes, A.V., Kazmierczak, K., Cheah, J.X., Gilda, J.E., Yuan, C.C., Zhou, Z., and Szczesna-Cordary, D. (2015). Proteomic analysis of physiological versus pathological cardiac remodeling in animal models expressing mutations in myosin essential light chains. J. Muscle Res. Cell Motil. *36*, 447–461. https://doi.org/10.1007/s10974-015-9434-0.

19. Bernardo, B.C., Weeks, K.L., Pretorius, L., and McMullen, J.R. (2010). Molecular distinction between physiological and pathological cardiac hypertrophy: experimental findings and therapeutic strategies. Pharmacol. Ther. *128*, 191–227. https://doi.org/10.1016/j.pharmthera.2010.04.005.

20. McMullen, J.R., and Jennings, G.L. (2007). Differences between pathological and physiological cardiac hypertrophy: novel therapeutic strategies to treat heart failure. Clin. Exp. Pharmacol. Physiol. *34*, 255–262. https://doi.org/10.1111/j.1440-1681.2007.04585.x.

21. Kazmierczak, K., Xu, Y., Jones, M., Guzman, G., Hernandez, O.M., Kerrick, W.G.L., and Szczesna-Cordary, D. (2009). The Role of the N-Terminus of the Myosin Essential Light Chain in Cardiac Muscle Contraction. J. Mol. Biol. *387*, 706–725. https://doi.org/10.1016/j.jmb.2009.02.006.

22. Aydt, E.M., Wolff, G., and Morano, I. (2007). Molecular modeling of the myosin-S1(A1) isoform. J. Struct. Biol. *159*, 158–163.

23. Wang, Y., Ajtai, K., Kazmierczak, K., Szczesna-Cordary, D., and Burghardt, T.P. (2016). N-Terminus of Cardiac Myosin Essential Light Chain Modulates Myosin Step-Size. Biochemistry *55*, 186–198. https://doi.org/10.1021/acs.biochem.5b00817.

24. Wang, Y., Yuan, C.C., Kazmierczak, K., Szczesna-Cordary, D., and Burghardt, T.P. (2018). Single cardiac ventricular myosins are autonomous motors. Open Biol. *8*, 170240. https://doi.org/10.1098/rsob.170240.

25. Michael, J.J., Gollapudi, S.K., Ford, S.J., Kazmierczak, K., Szczesna-Cordary, D., and Chandra, M. (2013). Deletion of 1-43 amino acids in cardiac myosin essential light chain blunts length dependency of Ca(2+) sensitivity and cross-bridge detachment kinetics. Am. J. Physiol. Heart Circ. Physiol. *304*, H253–H259. https://doi.org/10.1152/ajpheart.00572.2012.

26. Voigt, J.U., Pedrizzetti, G., Lysyansky, P., Marwick, T.H., Houle, H., Baumann, R., Pedri, S., Ito, Y., Abe, Y., Metz, S., et al. (2015). Definitions for a common standard for 2D speckle tracking echocardiography: consensus document of the EACVI/ASE/Industry Task Force to standardize deformation imaging. Eur. Heart J. Cardiovasc. Imag. *16*, 1–11. https://doi.org/10.1093/ehjci/jeu184.

27. Potter, E., and Marwick, T.H. (2018). Assessment of Left Ventricular Function by Echocardiography: The Case for Routinely Adding Global Longitudinal Strain to Ejection Fraction. JACC Cardiovasc. Imag. *11*, 260–274. https://doi.org/10.1016/j.jcmg.2017.11.017.

28. Kazmierczak, K., Yuan, C.-C., Liang, J., Huang, W., Rojas, A.I., and Szczesna-Cordary, D. (2014). Remodeling of the heart in hypertrophy in animal models with myosin essential light chain mutations. Front. Physiol. *5*, 353. https://doi.org/10.3389/fphys.2014.00353.

29. Rayment, I., Rypniewski, W.R., Schmidt-Bäse, K., Smith, R., Tomchick, D.R., Benning, M.M., Winkelmann, D.A., Wesenberg, G., and Holden, H.M. (1993). Three-dimensional structure of myosin subfragment-1: a molecular motor. Science *261*, 50–58.

30. Spudich, J.A. (2019). Three perspectives on the molecular basis of hypercontractility caused by hypertrophic cardiomyopathy mutations. Pflügers Archiv *471*, 701–717. https://doi.org/10.1007/s00424-019-02259-2.

31. Alamo, L., Ware, J.S., Pinto, A., Gillilan, R.E., Seidman, J.G., Seidman, C.E., and Padrón, R. (2017). Effects of myosin variants on interacting-heads motif explain distinct hypertrophic and dilated cardiomyopathy phenotypes. Elife *6*, e24634. https://doi.org/10.7554/eLife.24634.

32. Dutta, D., Nguyen, V., Campbell, K.S., Padrón, R., and Craig, R. (2023). Cryo-EM structure of the human cardiac myosin filament. Nature *623*, 853–862. https://doi.org/10.1038/s41586-023-06691-4.

33. Grinzato, A., Auguin, D., Kikuti, C., Nandwani, N., Moussaoui, D., Pathak, D., Kandiah, E., Ruppel, K.M., Spudich, J.A., Houdusse, A., and Robert-Paganin, J. (2023). Cryo-EM structure of the folded-back state of human beta-cardiac myosin. Nat. Commun. *14*, 3166. https://doi.org/10.1038/s41467-023-38698-w.

34. McNamara, J.W., Li, A., Dos Remedios, C.G., and Cooke, R. (2015). The role of super-relaxed myosin in skeletal and cardiac muscle. Biophys. Rev. *7*, 5–14. https://doi.org/10.1007/s12551-014-0151-5.

35. Yuan, C.C., Kazmierczak, K., Liang, J., Ma, W., Irving, T.C., and Szczesna-Cordary, D. (2022). Molecular basis of force-pCa relation in MYL2 cardiomyopathy mice: Role of the super-relaxed state of myosin. Proc. Natl. Acad. Sci. USA *119*, e2110328119. https://doi.org/10.1073/pnas.2110328119.

36. Yadav, S., Kazmierczak, K., Liang, J., Sitbon, Y.H., and Szczesna-Cordary, D. (2019). Phosphomimetic-mediated *in vitro* rescue of hypertrophic cardiomyopathy linked to R58Q mutation in myosin regulatory light chain. FEBS J. *286*, 151–168. https://doi.org/10.1111/febs.14702.

37. Mohran, S., Kooiker, K., Mahoney-Schaefer, M., Mandrycky, C., Kao, K., Tu, A.Y., Freeman, J., Moussavi-Harami, F., Geeves, M., and Regnier, M. (2024). The biochemically defined super relaxed state of myosin-A paradox. J. Biol. Chem. *300*, 105565. https://doi.org/10.1016/j.jbc.2023.105565.

38. Jani, V.P., Song, T., Gao, C., Gong, H., Sadayappan, S., Kass, D.A., Irving, T.C., and Ma, W. (2024). The structural OFF and ON states of myosin can be decoupled from the biochemical super- and disordered-relaxed states. PNAS Nexus *3*, pgae039. https://doi.org/10.1093/pnasnexus/pgae039.

39. Chang, A.N., Mahajan, P., Knapp, S., Barton, H., Sweeney, H.L., Kamm, K.E., and Stull, J.T. (2016). Cardiac myosin light chain is phosphorylated by Ca2+/calmodulin-dependent and -independent kinase activities. Proc. Natl. Acad. Sci. USA *113*, E3824–E3833. https://doi.org/10.1073/pnas.1600633113.

40. Szczesna-Cordary, D., and de Tombe, P.P. (2016). Myosin light chain phosphorylation, novel targets to repair a broken heart? Cardiovasc. Res. *111*, 5–7. https://doi.org/10.1093/cvr/cvw098.

41. Lord, S.J., Velle, K.B., Mullins, R.D., and Fritz-Laylin, L.K. (2020). SuperPlots: Communicating reproducibility and variability in cell biology. J. Cell Biol. *219*, e202001064. https://doi.org/10.1083/jcb.202001064.

42. Tamborrini, D., Wang, Z., Wagner, T., Tacke, S., Stabrin, M., Grange, M., Kho, A.L., Rees, M., Bennett, P., Gautel, M., et al. (2023). Structure of the native myosin filament in the relaxed cardiac sarcomere. Nature *623*, 863–871. https://doi.org/10.1038/s41586-023-06690-5.

43. Trayer, I.P., Trayer, H.R., and Levine, B.A. (1987). Evidence that the N-terminal region of A1-light chain of myosin interacts directly with the C-terminal region of actin. A proton magnetic resonance study. Eur. J. Biochem. *164*, 259–266.

44. Nyitrai, M., and Geeves, M.A. (2004). Adenosine diphosphate and strain sensitivity in myosin motors. Philos. Trans. R. Soc. Lond. B Biol. Sci. *359*, 1867–1877. https://doi.org/10.1098/rstb.2004.1560.

45. Anderson, R.L., Trivedi, D.V., Sarkar, S.S., Henze, M., Ma, W., Gong, H., Rogers, C.S., Gorham, J.M., Wong, F.L., Morck, M.M., et al. (2018). Deciphering the super relaxed state of human beta-cardiac myosin and the mode of action of mavacamten from myosin molecules to muscle fibers. Proc. Natl. Acad. Sci. USA *115*, E8143–E8152. https://doi.org/10.1073/pnas.1809540115.

46. Katti, P., Hall, A.S., Parry, H.A., Ajayi, P.T., Kim, Y., Willingham, T.B., Bleck, C.K.E., Wen, H., and Glancy, B. (2022). Mitochondrial network configuration influences sarcomere and myosin filament structure in striated muscles. Nat. Commun. *13*, 6058. https://doi.org/10.1038/s41467-022-33678-y.

47. Lee, E., May, H., Kazmierczak, K., Liang, J., Nguyen, N., Hill, J.A., Gillette, T.G., Szczesna-Cordary, D., and Chang, A.N. (2024). The MYPT2-regulated striated muscle-specific myosin light chain phosphatase limits cardiac myosin phosphorylation *in vivo*. J. Biol. Chem. *300*, 105652. https://doi.org/10.1016/j.jbc.2024.105652.

48. Hitsumoto, T., Tsukamoto, O., Matsuoka, K., Li, J., Liu, L., Kuramoto, Y., Higo, S., Ogawa, S., Fujino, N., Yoshida, S., et al. (2023). Restoration of Cardiac Myosin Light Chain Kinase Ameliorates Systolic Dysfunction by Reducing Superrelaxed Myosin. Circulation *147*, 1902–1918. https://doi.org/10.1161/CIRCULATIONAHA.122.062885.

49. Wang, Y., Xu, Y., Kerrick, W.G.L., Wang, Y., Guzman, G., Diaz-Perez, Z., and Szczesna-Cordary, D. (2006). Prolonged Ca2+ and force transients in myosin RLC transgenic mouse fibers expressing malignant and benign FHC mutations. J. Mol. Biol. *361*, 286–299. https://doi.org/10.1016/j.jmb.2006.06.018.

50. Schneider, C.A., Rasband, W.S., and Eliceiri, K.W. (2012). NIH Image to ImageJ: 25 years of image analysis. Nat. Methods *9*, 671–675. https://doi.org/10.1038/nmeth.2089.

51. Roy, A., Kucukural, A., and Zhang, Y. (2010). I-TASSER: a unified platform for automated protein structure and function prediction. Nat. Protoc. *5*, 725–738. https://doi.org/10.1038/nprot.2010.5.

52. National Research Council (2011). In Guide for the Care and Use of Laboratory Animals (National Academies Press).

53. Kanashiro-Takeuchi, R.M., Kazmierczak, K., Liang, J., Takeuchi, L.M., Sitbon, Y.H., and Szczesna-Cordary, D. (2022). Hydroxychloroquine Mitigates Dilated Cardiomyopathy Phenotype in Transgenic D94A Mice. Int. J. Mol. Sci. *23*, 15589. https://doi.org/10.3390/ijms232415589.

54. Yuan, C.C., Kazmierczak, K., Liang, J., Zhou, Z., Yadav, S., Gomes, A.V., Irving, T.C., and Szczesna-Cordary, D. (2018). Sarcomeric perturbations of myosin motors lead to dilated cardiomyopathy in genetically modified MYL2 mice. Proc. Natl. Acad. Sci. USA *115*, E2338–E2347. https://doi.org/10.1073/pnas.1716925115.

55. Yuan, C.C., Muthu, P., Kazmierczak, K., Liang, J., Huang, W., Irving, T.C., Kanashiro-Takeuchi, R.M., Hare, J.M., and Szczesna-Cordary, D. (2015). Constitutive phosphorylation of cardiac myosin regulatory light chain prevents development of hypertrophic cardiomyopathy in mice. Proc. Natl. Acad. Sci. USA *112*, E4138–E4146. https://doi.org/10.1073/pnas.1505819112.

56. Fiske, C.H., and Subbarow, Y. (1925). The colorimetric determination of phosphorus. J. Biol. Chem. *66*, 375–400.

57. Lee, E., Liu, Z., Nguyen, N., Nairn, A.C., and Chang, A.N. (2022). Myosin light chain phosphatase catalytic subunit dephosphorylates cardiac myosin via mechanisms dependent and independent of the MYPT regulatory subunits. J. Biol. Chem. *298*, 102296. https://doi.org/10.1016/j.jbc.2022.102296.

58. Zhang, Y. (2008). I-TASSER server for protein 3D structure prediction. BMC Bioinf. *9*, 40. https://doi.org/10.1186/1471-2105-9-40.

59. Roy, A., Yang, J., and Zhang, Y. (2012). COFACTOR: an accurate comparative algorithm for structure-based protein function annotation. Nucleic Acids Res. *40*, W471–W477. https://doi.org/10.1093/nar/gks372.

STAR★METHODS

KEY RESOURCES TABLE

REAGENT or RESOURCE	SOURCE	IDENTIFIER
Antibodies		
mouse monoclonal ELC antibody (Anti-Myosin light chain 3 antibody [MLM527])	Abcam	Cat#ab680; RRID:AB_2147601
goat anti-mouse antibody conjugated with fluorescent IRDye 800CW	Licor	Cat#926-32210; RRID:AB_621842
rabbit polyclonal RLC CT-1 antibody	Wang et al.[49]	N/A
goat anti-rabbit antibody IRDye 680RD	Licor	Cat#926-68071; RRID:AB_10956166
Chemicals, peptides, and recombinant proteins		
protease inhibitor cocktail	Sigma-Aldrich	Cat#P8340
2,3-Butanedione 2-monoxime (BDM)	Sigma-Aldrich	Cat#B-0753
Creatine Phosphokinase from rabbit muscle	Sigma-Aldrich	Cat# C3755-35KU
Creatine Phosphate	Sigma-Aldrich	Cat# 10621722001
mant-ATP	Thermo Fisher Scientific	Cat#M12417
Phenylmethylsulfonyl Fluoride	Sigma-Aldrich	Cat# 52332-25GM
Trichloroacetic acid	VWR	VW3372-1L
Critical commercial assays		
Coomassie Plus assay – The better Bradford Assay Kit	Thermo Fisher Scientific	Cat#23236
Experimental models: Organisms/strains		
Mouse: HCM-A57G ELC	Muthu et al.[12]	N/A
Mouse: RCM-E143K ELC	Yuan et al.[16]	N/A
Mouse: Δ43-ELC	Kazmierczak et al.[21]	N/A
Mouse: A57G X Δ43-ELC	This paper	N/A
Mouse: E143K X Δ43-ELC	This paper	N/A
Oligonucleotides		
Primer: Cross Forward: TGACAGACAGATCCCTCCTATCTC	This paper	N/A
Primer: Cross Reverse: ATAGGTGCCTGTGTCCTTGTTC	This paper	N/A
Software and algorithms		
Vevo LAB 5.6.1	FUJIFILM, Visual Sonics	https://www.visualsonics.com/product/software/vevo-lab
IonWizard	IonOptix, LLC	https://www.ionoptix.com/products/software/ionwizard-core-and-analysis/
ImageJ	Schneider et al.[50]	https://imagej.nih.gov/ij/
GraphPad PRISM version 7	GraphPad Software	https://www.graphpad.com/
I-TASSER-the secondary structure prediction	Roy et al.[51]	https://zhanggroup.org/I-TASSER/
Other		
Vevo 2100 ultrasound system equipped with an MS400 transducer	Visual Sonics	Vevo 2100
Odyssey Infrared Imaging System	LI-COR Biosciences	Model 9120
Zeiss Stereoscope Discovery.V12 equipped with AxioCam HRc (Zeiss) camera	Zeiss	Discovery.V12
Leitz microscope with Wetzlar objective (×40/0.65 NA) and AxioCam HRc (Zeiss) camera	Leitz	Dialux20
Guth Muscle Research System	Guth	N/A

Continued

REAGENT or RESOURCE	SOURCE	IDENTIFIER
IonOptix instrumentation equipped with hyper-switch dual excitation light source (with sub-millisecond switching times) and inverted fluorescence microscope with MyoCam-STM digital variable field rate CCD video system	IonOptix, LLC	N/A
Mixer-Mill MM301	Retsch GmbH	MM301

RESOURCE AVAILABILITY

Lead contact

Further information and requests for resources and reagents should be directed to and will be fulfilled by the lead contact, Danuta Szczesna-Cordary dszczesna@med.miami.edu.

Materials availability

Materials generated in this study are available from the lead contact upon request.

Data and code availability

- The published article includes all data generated or analyzed during this study.
- This paper does not report original codes.
- Any additional information required to reanalyze the data reported in this paper is available from the lead contact upon request.

EXPERIMENTAL MODEL AND STUDY PARTICIPANT DETAILS

Mouse models

This research adheres to the guidelines outlined in the Guide for the Care and Use of Laboratory Animals, as published by the US National Institutes of Health (NIH) (Publication No. 85–23, revised 2011).[52] All experimental procedures were subject to approval by the Institutional Animal Care and Use Committee at the University of Miami Miller School of Medicine, under protocol No. 21–106. This assurance was granted with the assurance number No. A-3224-01, valid until November 30, 2027. The humane euthanasia of the mice was performed through the administration of 100% carbon dioxide (CO_2) inhalation, followed by cervical dislocation. Briefly, mice were placed in a chamber gradually filled with CO_2 to achieve rapid unconsciousness (~2–3 min) with minimal distress to the animals. Following the exposure to CO_2, death was confirmed by employing a physical method (cervical dislocation), adhering to the recommendations provided in AVMA guidelines (AVMA Guidelines for the Euthanasia of Animals: 2020 Edition, https://www.avma.org/KB/Policies/Documents/euthanasia.pdf.

Transgenic mice

Previously generated transgenic HCM-A57G (HCM-mutant),[12] RCM-E143K (RCM-mutant),[16] and Δ43-ELC[21] on the B6SJL background mice were utilized to establish the A57G×Δ43 (HCM-truncated mutant) and E143K×Δ43 (RCM-truncated mutant) cross-genotype models. Various breeding strategies and combinations of lines and sexes were explored to achieve these models. The mouse lines included in the experiments were WT ELC (L1-76% transgene expression and L4-71%), HCM-mutant (L1-80% and L5-74%), RCM-mutant (L2-55%), and Δ43 (L8-34-39% and L9-35-40%) mice, as well as the cross-genotype models. Experiments were performed on 2-, 5-, and 8-month-old mice of both sexes.

METHOD DETAILS

Determination of transgene and protein expression in double mutant mice

The assessment of the double transgene in the offspring was performed using polymerase chain reaction (qPCR), employing a Forward Primer: 5′- TGACAGACAGATCCCTCCTATCTC -3′ and a Reverse Primer: 5′- ATAGGTGCCTGTGTCCTTGTTC -3′. These primers were specifically designed to detect the mutated ELC cDNA, which had been cloned into the SalI site of the plasmid referred to as α-myosin heavy chain (α-MHC) clone 26. This plasmid comprises approximately 5.5 kb of the mouse α-MHC promoter, encompassing the first two exons and part of the third exon, followed by the ELC sequence and a 630-bp 3′ untranslated region derived from the human growth hormone transcript. It is worth noting that the expected length of the PCR products was 436 bp, corresponding to the longer nucleotide sequence (A57G/E143K) and 307 bp for the Δ43 ELC sequence.

The expression of transgenic proteins was assessed in cardiac myofibrils (CMF) isolated from the hearts of mice approximately 8 months old, following previously established protocols.[11] Briefly, the hearts were excised, snap-frozen in liquid nitrogen, and stored at −80°C until

needed for experimentation. Upon thawing, the tissue was homogenized in CMF buffer (comprising 5 mM NaH_2PO_4, 5 mM Na_2HPO_4, pH 7.0, 0.1 mM NaCl, 5 mM $MgCl_2$, 0.5 mM EGTA, 5 mM ATP, 0.1% Triton X-100, 5 mM DTT, and 1 μL/mL protease inhibitor cocktail [P8340; Sigma-Aldrich]) using a Mixer-Mill MM301. Subsequently, the homogenate was centrifuged for 4 min at 2,000 x g, and the supernatant was discarded. After centrifugation, the pellets were left on ice for 2 min. This step was repeated three times using CMF buffer without Triton X-100. Finally, the pellets were resuspended in CMF buffer. Following determination of protein concentration via Coomassie Plus assay (Pierce, Rockford, IL, USA), the samples were mixed at a 1:1 ratio with Laemmli buffer and 5% β-mercaptoethanol (βME), then heated at 95°C for 5 min. Subsequently, the samples were loaded (approximately 10 μg/lane) and separated on 15% SDS-PAGE for Western blot analysis. Detection of the human ventricular light chain was facilitated by the distinct SDS-PAGE mobility of the human ventricular ELC (21,932 kDa) and Δ43 ELC (17,321 kDa) compared to the mouse ventricular ELC (22,421 kDa). Ventricular ELC protein was detected using a mouse monoclonal ELC ab680 antibody (Abcam, Cambridge, MA, USA), followed by a goat anti-mouse antibody conjugated with fluorescent IRDye 800CW (Licor, Lincoln, Nebraska, USA). Myosin regulatory light chain (RLC) was employed as a loading control and detected using a rabbit polyclonal RLC CT-1 antibody produced in our laboratory,[49] followed by a secondary goat anti-rabbit antibody IRDye 680RD (Licor, Lincoln, Nebraska, USA). Band intensities were analyzed using ImageJ software (https://imagej.nih.gov/ij/), and the percentage of transgenic ELC protein expression in HCM-truncated mutant and RCM-truncated mutant mice was calculated as previously described.[12]

Conventional and speckle tracking echocardiography (STE)

In vivo assessment of cardiac morphology and function in mice aged 2, 5, and 8 months was conducted using a Vevo 2100 ultrasound system (Visual Sonics, Toronto, ON, Canada) equipped with an MS400 transducer, following previously established protocols.[16,53,54] Heart images were acquired from anesthetized mice using isoflurane inhalation anesthesia (1–2%), ensuring heart rates (HR) remained above 400 beats/min and maintaining a body temperature of 37 ± 1°C. AutoLV analysis software (Vevo LAB 5.6.1, FUJIFILM, Visual Sonics, Toronto, ON, Canada) was employed to evaluate M-mode and B-mode images. The parameters assessed included LV inner diameter (LVID), LV posterior wall (LVPW), anterior walls (LVAW), LV mass, fractional shortening (FS), and ejection fraction (EF). High-resolution long-axis B-mode images, digitally stored as 300-frame cine loops, were utilized for speckle tracking echocardiography (STE) with the Vevo strain software (Vevo LAB 2.1.0). STE analyses were conducted using two-dimensional (B-mode) images in long- and short-axis views to measure global longitudinal strain (GLS), reflecting motion from the base to the apex along the long axis. Changes in length relative to the initial length were measured to characterize myocardial lengthening or shortening. Additionally, B-mode images were recorded, and vector diagrams were used to illustrate the magnitude and direction of endocardial deformation. Based on this analysis, global circumferential strain (GCS), which describes changes in the radius in the short axis, perpendicular to the radial axis, was computed.

Pulse-wave (PW) and tissue Doppler imaging (TDI)

PW and TDI were utilized to assess cardiac diastolic function. Doppler indexes, including the early (E) to late (A) filling velocity ratio of mitral inflow (E/A), isovolumetric contraction (IVCT), isovolumetric relaxation time (IVRT), ejection time (ET), and the subsequent calculation of the myocardial performance index (MPI), were measured according to established procedures.[13] TDI analysis was employed to visualize tissue movement, where negative waves indicated early diastolic myocardial relaxation (e′ velocity) and active atrial contraction during late diastole (a′ velocity). The mitral E/e′ ratio was also calculated to evaluate left ventricular filling pressure.

Morphometric heart analysis

Morphometric analysis of the heart included the evaluation of cardiac hypertrophy. Heart weight (HW) was measured relative to both tibia length (TL) and body weight (BW). Photographs of the whole hearts were taken using a Zeiss Stereoscope Discovery.V12 equipped with a 0.63×/5× PlanApo S objective and an AxioCam HRc (Zeiss) camera. Before imaging, the hearts underwent a quick rinse in ice-cold PBS to remove any excess blood.

Quantification of fibrosis by picrosirius red staining

To visualize and quantitatively assess fibrosis through histological means, Picrosirius Red Staining was performed at the Histology Laboratory of the University of Miami, Miller School of Medicine. The hearts were longitudinally sectioned, with the posterior sections designated for histological analysis. Five images were captured per LV section, representing approximately three animals per group, and these images were averaged. The imaging was conducted using a Leitz Wetzlar objective (×40/0.65 NA) and an AxioCam HRc camera (Zeiss) mounted on a light Dialux20 microscope. The quantification of fibrosis, expressed as a percentage, was determined by measuring the Sirius Red intensity and normalizing it to the total myocardial area using ImageJ.

Electron microscopy

Transmission Electron Microscopy (TEM) was utilized to assess the overall sarcomere morphology and ultrastructure, and this analysis was conducted at the EM Core Facility at the University of Miami, Miller School of Medicine. After euthanasia, the hearts were swiftly excised, rinsed with ice-cold PBS, and immersed in a solution containing 10–12% paraformaldehyde overnight. Subsequently, the anterior portion of each heart was divided into the left ventricle and septum, and the slides were examined using a Philips CM-10 electron microscope at

magnifications of 1000×, 3000x, and 5000x. The number and size of mitochondria were evaluated at the 3000× objective using ImageJ. It's important to note that one female mouse from each group was included in this study.

Steady state maximal force and calcium sensitivity measurements

Left ventricular papillary muscle (LVPM) fibers were isolated from the hearts of mice and dissected into small muscle bundles (2–3 mm in length and 0.5–1 mm in diameter) in ice-cold pCa 8 solution (containing 10^{-8} M [Ca^{2+}], 1 mM free [Mg^{2+}] [total MgPr (propionate = 3.88 mM], 7 mM EGTA, 2.5 mM [Mg-ATP^{2-}], 20 mM MOPS pH 7.0, 15 mM creatine phosphate, and 15 U/mL of phosphocreatine kinase (Sigma-Aldrich, St. Louis, MO, USA)). The ionic strength was adjusted to 150 mM using KPr. Additionally, the solution contained 30 mM 2,3-Butanedione 2-monoxime (BDM) and 15% glycerol, and the muscle bundles were incubated for approximately 1 h on ice. Subsequently, the muscle strips were chemically skinned by immersing them in a solution containing 1% Triton X-100, added to the mixture of pCa 8 solution and 50% glycerol (storage solution), overnight at 4°C. After this incubation, the bundles were transferred to a new storage solution without Triton and kept at −20°C for 5–10 days.[16,54,55]

On the day of the experiment, small muscle strips, typically consisting of approximately three to six single muscle fibers, were isolated from a batch of glycerinated skinned LVPM bundles and attached to the force transducer of the Guth Muscle Research System (Heidelberg, Germany). They were soaked in a pCa 8.0 solution containing 1% Triton X-100 for 30 min and then rinsed in pCa 8 buffer. Subsequently, the fibers were immersed in the pCa 4 solution, which had the same composition as the pCa 8 solution except for a [Ca^{2+}] of 10^{-4} M, to establish the maximal level of force. After maximal force was determined, the strips were relaxed in pCa 8 and exposed to solutions with increasing concentrations of Ca^{2+} (ranging from pCa 8 to 4), thereby establishing the force-pCa relationship. Data obtained were analyzed using the Hill equation, where "[Ca^{2+}]$_{50}$ or pCa$_{50}$" denotes the free Ca^{2+} concentration required to produce 50% of the maximum force.[35]

Myofibrillar (MF) ATPase activity assays

Cardiac myofibrils preparation

Skinned mouse cardiac myofibrils (MCMFs) were prepared from the ventricles of 2–3 mice (both sexes), aged around 6–11 months, as described previously.[21] All solutions used for the MCMFs preparation contained 1 mM DTT, 1 mM phenylmethylsulfonyl fluoride (PMSF), and a protease inhibitor cocktail. Ventricular tissue was minced in 300 mM sucrose with 10 mM imidazole (pH 7), then homogenized with a stainless steel ball in a Retsch M300 Mixer Mill for 2 min at 24 Hz. After homogenization, the samples were centrifuged for 1 min at 1500 g. The pellet was treated again with the sucrose solution, followed by a second homogenization (2 min at 27 Hz) and centrifugation. Next, the samples were washed with 2 mM EGTA in standard CMF buffer (30 mM MOPS, pH 7.0, 60 mM KCl, 2 mM MgCl$_2$). After centrifugation, the samples were washed three times with 1% Triton X-100, with each wash followed by a 30-min incubation on ice. The samples were then washed four times with CMF buffer mixed with glycerol. The first wash was done with 25% glycerol, and the following three washes were done with 50% glycerol. The isolated MCMFs were stored at −20°C until the time of the ATPase assay.

MF ATPase assay

MF ATPase activity assays using all groups of Tg ELC mouse models were performed under two conditions: +Ca^{2+} (maximal activity) and −Ca^{2+} (basal activity). The reaction buffers were composed of 70 mM KCl, 1 mM MgCl$_2$, 20 mM imidazole (pH 7), 1 mM DTT, and 0.5 mM CaCl$_2$ for +Ca^{2+}, or 1 mM EGTA for −Ca^{2+}.[21] 10-μg myofibrillar samples, suspended in a solution of 20 mM MOPS (pH 7.0), 40 mM KCl, and 2.5 mM MgCl$_2$, were added to the reaction buffer. After 5 min of incubation at 25°C, the ATPase reaction was initiated with the addition of 2.5 mM ATP and terminated after 10 min with 5% trichloroacetic acid. Released inorganic phosphate was measured according to the method of Fiske and Subbarow.[56] Myofibrillar activity was calculated and expressed as μmol phosphate/mg MCMF/min.

Mant-ATP chase experiments

Mant-ATP assays were conducted on skinned LVPM fibers using IonOptix instrumentation, following the procedures outlined in.[13,35] In brief, fibers were immersed in a rigor solution (120 mM KPr, 5 mM MgPr, 2.5 mM K$_2$HPO$_4$, 2.5 mM KH$_2$PO$_4$, 50 mM MOPS, pH 6.8, and fresh 2 mM DTT) containing 250 μM mantATP. After fluorescence stabilized (3–5 min), the fibers were treated with 4 mM non-labeled ATP and fluorescence decay versus time isotherms were recorded. Decay curves were fitted to a two-state exponential equation to derive the amplitudes of the fast (P1) and slow (P2) phases of fluorescence decay and their respective T1 and T2 lifetimes (in seconds). To estimate the percentage of the DRX versus SRX states, a competition assay was conducted to correct for non-specific mant-ATP binding in LVPM fibers.[35] In brief, the fibers were incubated in 250 μM mantATP with varied concentrations of ATP. The obtained fluorescence was normalized to the fluorescence in the absence of added ATP and plotted as a function of added [ATP]. The data were fitted to a competition model, Intensity = I_{NS} + (1 − I_{NS})/ ([ATP]·K_{app}ATP/[mATP]·K_{app}mATP + 1), where I_{NS} represents the intensity due to nonspecific binding. These ATP-titration experiments, performed on skinned cardiac fibers yielded the fraction of nonspecifically bound mantATP, as 0.44 ± 0.02 (SEM). The percentage of the SRX state was then calculated as P2/(1–0.44)*100% and the DRX state as 100-SRX%.[35]

Assessment of protein phosphorylation

Analysis of RLC protein phosphorylation was conducted on urea protein extracts, prepared following the procedure outlined in Lee et al.[57] Approximately 30–60 mg of LV tissue, frozen in liquid nitrogen and stored at −80°C until use, was ground into a uniform heart powder while

still in liquid nitrogen. Subsequently, it was simultaneously thawed and precipitated in a solution containing 10% trichloroacetic acid and 10 mM dithiothreitol. The resulting precipitated tissue granules were washed with ethyl ether (three washes of 10 min each), air-dried briefly to evaporate the ether, and then suspended in approximately 30 times the volume of the urea sample buffer. This buffer consisted of 8 M urea, 20 mM Tris (pH 8.6), 23 mM glycine, 10 mM dithiothreitol, and 4 mM EDTA. The samples were agitated on a platform shaker for approximately 6 h at room temperature, with the addition of urea crystals to saturation, until the proteins were fully solubilized. Subsequently, the samples were centrifuged at 10,000 × g for 2 min. The resulting protein extracts were subjected to protein concentration assessment using the Coomassie Plus assay (Thermofisher Scientific, Waltham, MA USA). Then, samples of approximately 100 μL each were mixed with 70 mg of urea crystals, 10 μL of β-mercaptoethanol (βME), and 5 μL of bromophenol blue. These prepared samples (∼10 μg/lane) were subjected to urea-polyacrylamide gel electrophoresis (urea-PAGE) using a 12% polyacrylamide gel in the presence of 8 M urea and subjected to 110V of electric current. Subsequently, Western blotting was performed using a rabbit polyclonal RLC CT-1 antibody. Intensities of the separated bands corresponding to phosphorylated and nonphosphorylated RLCs were quantified using ImageJ software. The extent of endogenous RLC phosphorylation was then calculated as phosphorylated RLC/total RLC protein.

Secondary structure prediction

The secondary structure prediction of WT, Δ43, HCM-mutant, and RCM-mutant ELC proteins was performed using the I-TASSER software, which is available as an online server at https://zhanggroup.org/I-TASSER/.[51] Initially, the amino acid sequences were aligned with template proteins exhibiting similar structures sourced from the PDB library. Subsequently, the complete protein structures were reconstructed from these aligned fragments and subjected to simulation, utilizing specific algorithms to derive the model with the lowest energy. Each predicted model's confidence level was assessed via a C-score, ranging from −5 to 2, wherein higher scores denoted superior prediction quality.[51,58,59] The structures with the highest confidence scores were subsequently modeled using the PyMOL molecular visualization system, accessible at https://pymol.org/2/.

QUANTIFICATION AND STATISTICAL ANALYSIS

All values are presented as mean ± SD (standard deviation). Differences between multiple groups were assessed using one-way ANOVA followed by Tukey's multiple comparisons test. Specific differences between mutants were calculated using Student's t test, with significance defined as $p < 0.05$ (GraphPad Prism 7.05).